NASA Technical Memorandum 89044

Measured Pressure Distributions Inside Nonaxisymmetric Nozzles With Partially Deployed Thrust Reversers

Robert S. Green and George T. Carson, Jr.

MARCH 1987

NASA

NASA Technical Memorandum 89044

Measured Pressure Distributions Inside Nonaxisymmetric Nozzles With Partially Deployed Thrust Reversers

Robert S. Green
Wright-Patterson Air Force Base
Dayton, Ohio

George T. Carson, Jr.
Langley Research Center
Hampton, Virginia

National Aeronautics
and Space Administration

**Scientific and Technical
Information Branch**

1987

Summary

An investigation was conducted in the Langley 16-Foot Transonic Tunnel at static conditions to measure the pressure distributions inside a nonaxisymmetric nozzle with simultaneous partial thrust reversing (50-percent deployment) and thrust vectoring of the primary (forward-thrust) nozzle flow. Geometric forward-thrust-vector angles of 0° and 15° were tested. These nozzles were installed on a model of a generic twin-engine fighter aircraft. High-pressure air was used to simulate jet exhaust. Test data were obtained at static conditions while nozzle pressure ratio was varied from 2.0 to 4.0.

The three-dimensional nature of internal exhaust flow in a nonaxisymmetric nozzle was indicated by variations in pressure between the nozzle flaps and the sidewall. Additionally, a complicated, asymmetric exhaust flow pattern was evident in the primary-flow exhaust duct of the 15° vectored nozzle.

Introduction

Mission requirements for the next generation of fighter aircraft may necessitate a vehicle with high maneuverability and short take-off and landing (STOL) capability. Such an aircraft will probably be equipped with multifunction nozzles which will have thrust-reversing and thrust-vectoring capabilities. Both axisymmetric and nonaxisymmetric nozzle concepts have been studied. The nonaxisymmetric, thrust-reversing, thrust-vectoring nozzle offers the possible advantage of a lower installed weight penalty when compared with an advanced axisymmetric nozzle having the same functions (refs. 1 to 3).

In addition to an experimental data base which provides propulsive performance characteristics, studies have provided details of the nozzle internal flow fields (refs. 4 to 6). Still, there is much to be learned about the internal flow of nonaxisymmetric nozzles. A knowledge of the internal flow phenomena is needed for improved nozzle designs. Furthermore, the development of accurate numerical procedures which predict the flow inside a nonaxisymmetric nozzle requires an understanding of the physical characteristics of the flow field.

The purpose of this investigation is, therefore, to provide detailed static-pressure measurements of the flow inside two nonaxisymmetric nozzle configurations with partially deployed thrust reversers. The two configurations were identical except the primary nozzle flow was unvectored for one configuration and was pitch vectored 15° for the other. Performance data for these nozzles are presented in reference 7. The investigation was conducted in the Langley 16-Foot Transonic Tunnel (ref. 8) at static conditions ($M = 0$) while nozzle pressure ratio was varied from 2.0 to 4.0.

Symbols

M	Mach number
NPR	nozzle pressure ratio, $p_{t,j}/p_a$
p	local static pressure, psia
p_a	ambient pressure, psia
$p_{t,j}$	jet total pressure, psia
w	vertical coordinate, in. (see fig. 5(a))
w_t	vertical distance from nozzle centerline to upper nozzle wall at nozzle entrance, 1.050 in. (see fig. 5(a))
x	axial coordinate, in. (see fig. 5(a))
x'	surface coordinate starting at internal surface break points (see fig. 5(c))
x_t	axial distance from nozzle entrance to primary nozzle throat, 1.595 in. (see fig. 5(a))
y	lateral coordinate perpendicular to nozzle centerline, in. (see fig. 5(c))
η	perpendicular to line of pressure orifices in coordinate system obtained by 15° downward rotation of nozzle centerline, in. (see fig. 5(b))
η_t	perpendicular distance in coordinate system measured from 15° vectored nozzle centerline to nozzle flap, 0.221 in. (see fig. 5(b))

Abbreviations:

BL	buttock line, in.
FS	fuselage station, in.
NS	nozzle station, in.
WL	waterline, in.

Apparatus and Procedure

Wind Tunnel

This investigation was conducted in the Langley 16-Foot Transonic Tunnel. The free-stream Mach number was zero and the wind tunnel was used only as a static test facility.

Twin-Jet-Propulsion Simulation System

The two nozzle configurations tested were installed on a portion of a wing-tip-supported model

of a generic twin-engine fighter aircraft. A sketch of the aircraft model (without empennage surfaces) and the support system is shown in figure 1. A photograph of the test setup is shown in figure 2. The external forebody shell, the centerbody top shell, and the afterbody shell were removed for this investigation since external flow was not present. A more complete description of the wing-tip model support system is contained in references 7 and 8.

For jet-propulsion simulation, the Langley 16-Foot Transonic Tunnel is equipped with an external high-pressure air system which provides a continuous flow of clean, dry air at a nominal controlled temperature of 540°R ahead of the nozzle throat. Two remotely operated flow-regulating valves are used to balance the jet total pressure in the left and right nozzles. The airflow path can be traced from the sketches in figure 1. Compressed air flows through the two wing-tip support booms, then through each wing panel into two high-pressure plenums on each side of the fuselage. The air is then discharged, perpendicular to the model axis, through eight equally spaced sonic nozzles in each high-pressure plenum. Next, the airflow passes successively through a tailpipe, a circular-to-rectangular transition section, a choke plate, and an instrumentation section, and then expands through the nozzle configuration being tested.

Nozzle Models

The two nozzle configurations used in the current investigation were part of a test matrix of nozzle configurations previously evaluated for aeropropulsive performance (ref. 7). These configurations were designed to simulate various percentages of thrust-reverser deployment of twin dry-power, nonaxisymmetric, convergent-divergent nozzles having a design NPR of approximately 3.5. One of the nozzle design values held constant during this investigation was total nozzle throat area; that is, the sum of the primary-flow throat area and the reverser-port throat area was held constant. (Total nozzle throat area was independent of reverser deployment.) In a full-scale operational nozzle of the current design, thrust reversal is achieved by rotation of the top and bottom convergent and divergent flaps such that primary flow is gradually blocked while the forward-facing reverser ports are opened. The convergent and divergent flaps are independently actuated such that the divergent flaps can be rotated for thrust vectoring of the remaining primary nozzle flow (for reversers deployed less than 100 percent).

In the current investigation, two nozzle configurations simulating 50-percent reverser deployment were tested. Reverser deployment of 50 percent means that half of the original total throat area is diverted to the reverser ports and the remaining half is used for the primary (forward-thrust) exhaust flow. One nozzle configuration had unvectored primary flow (thrust-vector angle equal to 0°), and the other configuration had vectored primary flow (thrust-vector angle equal to 15°). Sketches of these two configurations are shown in figure 3. Photographs showing the nozzle configuration with the reverser deployed 50 percent and primary flow vectored 15° are shown in figure 4.

Instrumentation

Jet stagnation conditions were measured in an instrumentation section upstream of each nozzle. (See fig. 1.) A four-probe rake was used to measure jet total pressures, and the average of these measurements was used in the computation of the nozzle pressure ratio NPR and the nozzle static-pressure ratio $p/p_{t,j}$. Jet total temperature was measured with a single thermocouple probe located in each instrumentation section. Static-pressure orifice locations on the internal surfaces of the nozzle flaps and sidewall are shown in the photographs of figure 4 and in the sketches of figure 5. Coordinates of the nozzle static-pressure orifice locations are given in table I. Fifty-six static-pressure orifices were located on the internal sidewall surface of the 0° vectored nozzle (see fig. 5(a)), and 55 static-pressure orifices were located on the internal sidewall surface of the 15° vectored nozzle (see fig. 5(b)). The nozzle upper flaps for the 0° vectored (fig. 5(c)) and 15° vectored (fig. 5(d)) configurations each had 15 static-pressure orifices. Nine static-pressure orifices were located on the lower divergent flap of the 15° vectored nozzle (fig. 5(e)). As indicated in figure 5 and table I, some of the orifices on the upper flap were positioned slightly off of the flap centerline, as necessitated by installation of pressure instrumentation. Data obtained from these orifices are presented undistinguished from the data from the flap centerline since the flow is assumed to be essentially two dimensional near the nozzle centerline.

Tests and Data Reduction

This investigation was conducted in the Langley 16-Foot Transonic Tunnel at static conditions. Nozzle pressure ratio was varied from 2.0 to approximately 4.0. Test data were recorded on magnetic tape with the Langley 16-Foot Transonic Tunnel data acquisition system. At each test point, 50 samples of data were taken over a 5-sec period. The average value of these samples was used for computation.

Presentation of Results

Nozzle internal static-pressure distributions are presented in figure 6 for the 0° vectored nozzle and in figure 7 for the 15° vectored nozzle. Pressure data are shown as the ratio of local static pressure to jet total pressure $p/p_{t,j}$ as a function of the nozzle downstream distance nondimensionalized by the distance from the entrance of the nozzle to the primary nozzle throat x/x_t. (See fig. 5(a).) In figure 6(c), the ratio w/w_t represents the nondimensionalized sidewall height. (See fig. 5(a).) In figure 7(d), the ratio η/η_t represents the nondimensionalized primary-exhaust-duct height. (See fig. 5(b).) Static-pressure-ratio data are presented in table II. For the 0° vectored nozzle, these data are given at the locations defined by x/x_t and w/w_t. For the 15° vectored nozzle, these data are given at the locations defined by x/x_t, w/w_t, and η/η_t.

Figure 8 presents sketches illustrating some of the internal flow phenomena which are indicated by the static-pressure distributions. No attempt was made to scale these phenomena (location or magnitude) on these sketches.

Discussion

0° Vectored Nozzle

Figure 6 presents internal static-pressure data for the 0° vectored primary-flow nozzle configuration. Figure 8(a) presents a sketch of the hypothesized internal flow phenomena based on these data. The upper flap centerline pressures on the 0° vectored nozzle (fig. 6(a)) show little variation with NPR. However, the sidewall centerline ($w/w_t = 0$) pressures (fig. 6(b)) are slightly dependent on NPR for NPR < 3.02. These observations indicate the nozzle exhaust flow has certain three-dimensional qualities. Since the primary flow exhausts through a constant-area duct, a second choke point may exist for the primary flow at the exit because of boundary-layer growth in the duct. In this case, the primary-flow constant-area duct acts as a supersonic diffuser, and this would account for both the relative independence of flap static pressure with NPR and the rise in flap static pressure as the duct exit is approached ($p/p_{t,j} = 0.528$ for $M = 1.0$). In any event, the design NPR for a nozzle having equal throat and exit areas is 1.89, and all the data from the current investigation were obtained at underexpanded nozzle operating conditions (NPR > 1.89). This fact by itself would cause the nozzle flap static pressures to be independent of NPR (ref. 9).

A stagnation region ($p \approx p_{t,j}$) on the primary-flow convergent surface is shown in figure 6(a) from $x/x_t \approx 0.75$ to $x/x_t \approx 0.82$. A strong expansion occurs on either side of the stagnation region as the flow approaches the reverser-port throat (decreasing x/x_t from stagnation point) and the throat of the primary-flow constant-area duct (increasing x/x_t from stagnation point). As indicated by the static-pressure distributions of figure 6(a), expansion of the primary exhaust flow continues past the constant-area duct entrance ($x/x_t = 1.00$); the sonic line ($p/p_{t,j} = 0.528$ for $M = 1.0$) appears to be located at $x/x_t \approx 1.07$. A separation bubble may be associated with the strong expansion around the sharp corner of the constant-area duct entrance. A short distance downstream of the sonic line (possibly at the separation reattachment point), a shock or strong compression results in a rapid increase in static pressure, which is followed by additional supersonic flow expansion. For $x/x_t > 1.50$, there is a gradual rise in static pressure, which is characteristic of supersonic flow in a convergent duct. Boundary-layer growth in the constant-area duct would account for this effect. As noted previously, the constant-area duct may be acting as a supersonic diffuser and a second sonic line may exist at the duct exit. Figure 8(a) presents a sketch illustrating some of the flow phenomena on the upper flap discussed above. It is assumed that, because of model symmetry, flow on the lower flap is identical to that on the upper flap.

Static-pressure distributions along the sidewall centerline ($w/w_t = 0$; see fig. 6(b)), unlike those on the upper flap, show no evidence of a shock or strong compression. (See fig. 8.) Examination of figure 6(c) shows that the sidewall static-pressure distribution varies as flow on the sidewall approaches the upper wall of the constant-area duct. At $w/w_t = 0.095$ (upper wall of constant-area duct located at $w/w_t = 0.210$), a weak shock may be present near $x/x_t \approx 1.40$. The above results again illustrate three-dimensional flow effects in a nonaxisymmetric (two-dimensional) nozzle. The sidewall static-pressure-ratio contours shown in figure 6(d) illustrate the stagnation region on the primary-flow convergent surface and the rapid expansion at the corner of the entrance to the primary-flow constant-area duct discussed previously.

15° Vectored Nozzle

Figure 7 presents internal static-pressure data for the nozzle configuration with the primary-flow pitch thrust vectored 15°. Figure 8(b) presents a sketch of the hypothesized internal flow phenomena for this configuration. For the range of nozzle pressure ratios of this investigation, all the data presented for this configuration are at underexpanded nozzle operating conditions. Similar to the 0° vectored nozzle,

flap static pressures on the 15° vectored nozzle are essentially independent of nozzle pressure ratio (see figs. 7(a) and 7(b)). Sidewall centerline pressures of the 15° vectored nozzle (fig. 7(c)) show less sensitivity to NPR than those noted previously for the 0° vectored nozzle (fig. 6(b)).

The static-pressure data obtained on the 15° vectored nozzle configuration indicate internal flow phenomena (fig. 8(b)) similar to that discussed previously for the 0° vectored nozzle (fig. 8(a)). The flow phenomena shown in figure 8(b) are hypothesized from the pressure data, and other flow phenomena may explain the same static-pressure distribution trends. For example, an extreme thickening of the boundary layer could result in the same trends as those associated with the separation bubble hypothesized in figure 8. In addition, the sharp rises in static pressure on the upper and lower walls of the primary-flow constant-area duct (figs. 7(a) and 7(b)) shown in figure 8(b) as individual shocks or compressions could also be caused by a single shock which originates on the lower wall just downstream of the sonic line ($x/x_t \approx 1.10$), reflects off the upper wall ($x/x_t \approx 1.45$), and again strikes the lower wall ($x/x_t \approx 1.58$). However, individual shocks or compressions are shown in figure 8(b) because the sidewall centerline static-pressure distributions (fig. 7(c)) do not indicate passage of a compression wave. The static-pressure distribution presented in figure 7(a) indicates the possibility of a shock wave at $x/x_t \approx 1.44$ on the upper flap. Figure 7(b) indicates the possibility of shock waves at $x/x_t \approx 1.58$. Also, the sidewall static-pressure distribution closer to the lower flap (fig. 7(d), $\eta/\eta_t = -0.452$) tends to confirm the presence of two shock waves on the lower flap.

The most striking similarity between the static-pressure distributions of the 15° vectored and 0° vectored configurations is the existence of a stagnation region on the primary-flow convergent-flap surface. (Compare figs. 6(a) and 6(d) with figs. 7(a) and 7(e).) The most striking dissimilarity between the two data sets is the asymmetry of the flow in the constant-area duct of the 15° vectored nozzle configuration. Static-pressure distributions on the upper flap of the 15° vectored nozzle (fig. 7(a)) show no indication of a separation bubble near the duct entrance, whereas a large separation bubble is hypothesized on the lower flap (fig. 7(b)). Although a compression (shock) wave could account for the sharp increase in static pressure on the lower flap from $x/x_t \approx 1.10$ to $x/x_t \approx 1.35$, the large range of x/x_t over which this static-pressure rise is "smeared" more likely is explained by the normal supersonic flow deceleration which occurs in a converging duct. A converging duct in this case is caused by the large separation bubble (or thick boundary layer) on the lower flap. The separation bubble on the upper flap of the 0° vectored nozzle (fig. 8(a)) has been eliminated on the upper flap of the 15° vectored nozzle because less flow turning is required. Conversely, the separation bubble on the lower flap of the 15° vectored nozzle is much larger than that on the lower flap of the 0° vectored nozzle because more flow turning is required during vectored-thrust operation. Other signs of flow asymmetry in the vectored-thrust, constant-area duct are location of the sonic line ($x/x_t \approx 1.20$ on the upper flap and $x/x_t < 1.10$ on the lower flap) and location of the shock or compression waves ($x/x_t \approx 1.44$ on the upper flap and $x/x_t \approx 1.25$ and $x/x_t \approx 1.58$ on the lower flap). The existence of a second sonic line at the 15° vectored nozzle exit is not shown in figure 8(b) since, unlike the 0° vectored nozzle, static pressures on both the upper and lower flaps indicate additional expansion (downstream of last shock or compression) as the exit is approached.

Concluding Remarks

An investigation has been conducted in the Langley 16-Foot Transonic Tunnel to measure static-pressure distributions inside a nonaxisymmetric nozzle with simultaneous partial thrust reversing (50-percent deployment) and thrust vectoring of the primary (forward-thrust) nozzle flow. Geometric forward-thrust-vector angles of 0° and 15° were tested. Test data were obtained at static conditions while nozzle pressure ratio was varied from 2.0 to 4.0.

The three-dimensional nature of internal exhaust flow in a nonaxisymmetric nozzle was indicated by variations in pressure between the nozzle flaps and the sidewalls. Additionally, a complicated asymmetric exhaust flow pattern was evident in the primary-flow exhaust duct of the 15° vectored nozzle which was not evident for the 0° vectored nozzle.

NASA Langley Research Center
Hampton, Virginia 23665-5225
December 31, 1986

References

1. Capone, Francis J.: The Nonaxisymmetric Nozzle—It Is for Real. AIAA Paper 79-1810, Aug. 1979.
2. Dusa, D. J.; Speir, D. W.; Rowe, R. K.; and Leavitt, L. D.: Advanced Technology Exhaust Nozzle Development. AIAA-83-1286, June 1983.
3. Dusa, D. J.; Speir, D. W.; and Dunbar, D. K.: Multi-Functional Nozzle for Advanced Weapon Systems. *SAE 1983 Transactions*, Section 4, Volume 92, Soc. of Automotive Engineers, Inc., c.1984, pp. 4-54–4-64. (Available as SAE Paper 831426.)
4. Mason, Mary L.; Putnam, Lawrence E.; and Re, Richard J.: *The Effect of Throat Contouring on Two-Dimensional Converging-Diverging Nozzles at Static Conditions.* NASA TP-1704, 1980.
5. Putnam, Lawrence E.; and Strong, Edward G.: *Internal Pressure Distributions for a Two-Dimensional Thrust-Reversing Nozzle Operating at a Free-Stream Mach Number of Zero.* NASA TM-85655, 1983.
6. Re, Richard J.; and Leavitt, Laurence D.: *Static Internal Performance Including Thrust Vectoring and Reversing of Two-Dimensional Convergent-Divergent Nozzles.* NASA TP-2253, 1984.
7. Carson, George T., Jr.; Capone, Francis J.; and Mason, Mary L.: *Aeropropulsive Characteristics of Nonaxisymmetric-Nozzle Thrust Reversers at Mach Numbers From 0 to 1.20.* NASA TP-2306, 1984.
8. Peddrew, Kathryn H., compiler: *A User's Guide to the Langley 16-Foot Transonic Tunnel.* NASA TM-83186, 1981.
9. Shapiro, Ascher H.: *The Dynamics and Thermodynamics of Compressible Fluid Flow. Volume I.* Ronald Press Co., c.1953.

Table I. Internal Static-Pressure Orifice Locations

(a) Sidewall surface for 0° vectored primary flow (see fig. 5(a))

		w, in.									
		0	0.100	0.230	0.360	0.490	0.620	0.750	0.880	0.980	1.080
		w/w_t									
x, in.	x/x_t	0	0.095	0.219	0.343	0.467	0.590	0.714	0.838	0.933	1.029
0.595	0.373						×	×	×		
.645	.404	×			×	×	×	×	×		
.795	.498	×			×	×	×	×	×	×	×
.895	.561		×	×	×	×	×	×		×	×
.995	.624	×	×	×	×	×		×	×	×	×
1.195	.749	×	×	×	×	×					
1.345	.843		×	×	×						
1.395	.875	×									
1.495	.937	×	×								
1.695	1.063		×								
1.790	1.122	×									
1.845	1.157		×								
1.940	1.216	×									
2.095	1.313		×								
2.190	1.373	×									
2.345	1.470		×								
2.440	1.530	×									
2.595	1.627		×								
2.690	1.687	×									
2.940	1.843	×									

Table I. Continued

(b) Sidewall surface for 15° vectored primary flow (see fig. 5(b))

		w, in.									
		0	0.100	0.230	0.360	0.490	0.620	0.750	0.880	0.980	1.080
		w/w_t									
x, in.	x/x_t	0	0.095	0.219	0.343	0.467	0.590	0.714	0.838	0.933	1.029
0.595	0.373						×	×	×		
.645	.404	×			×	×	×	×	×		
.795	.498	×			×	×	×	×	×	×	×
.895	.561		×	×	×	×	×	×		×	×
.995	.624	×	×	×	×	×		×	×	×	×
1.195	.749	×	×	×	×	×					
1.345	.843		×	×							
1.395	.875	×									
1.495	.937	×	×								

		η, in.	
		0	−0.100
		η/η_t	
x, in.	x/x_t	0	−0.452
1.666	1.045		×
1.692	1.061	×	
1.810	1.135		×
1.837	1.152	×	
2.052	1.287		×
2.078	1.303	×	
2.293	1.438		×
2.320	1.455	×	
2.535	1.589		×
2.561	1.606	×	
2.805	1.759	×	

Table I. Continued

(c) Upper flap surface for 0° vectored primary flow; NS 1.095 to NS 1.143 (see fig. 5(c))

x', in.	x, in.	x/x_t	y, in. 0.125
0.120	1.105	0.693	×
.240	1.116	.700	×
.360	1.126	.706	×

(d) Upper flap surface for 0° vectored primary flow; NS 1.143 to NS 1.595 (see fig. 5(c))

x', in.	x, in.	x/x_t	y, in. −0.125
0.120	1.217	0.763	×
.240	1.291	.809	×
.360	1.365	.856	×
.480	1.438	.902	×
.600	1.512	.948	×

(e) Upper flap surface for 0° vectored primary flow; NS 1.595 to NS 3.049 (see fig. 5(c))

x', in.	x, in.	x/x_t	y, in. 0
0.120	1.715	1.075	×
.240	1.835	1.150	×
.360	1.955	1.226	×
.720	2.315	1.451	×
.840	2.435	1.527	×
1.080	2.675	1.677	×
1.200	2.795	1.752	×

Table I. Continued

(f) Upper flap surface for 15° vectored primary flow; NS 1.095 to NS 1.143 (see fig. 5(d))

x', in.	x, in.	x/x_t	y, in. 0.125
0.120	1.105	0.693	×
.360	1.126	.706	×

(g) Upper flap surface for 15° vectored primary flow; NS 1.143 to NS 1.595 (see fig. 5(d))

x', in.	x, in.	x/x_t	y, in. −0.125
0.120	1.217	0.763	×
.240	1.291	.809	×
.360	1.365	.856	×
.480	1.438	.902	×
.600	1.512	.948	×

(h) Upper flap surface for 15° vectored primary flow; NS 1.595 to NS 3.049 (see fig. 5(d))

x', in.	x, in.	x/x_t	y, in. 0
0.120	1.711	1.073	×
.240	1.827	1.145	×
.360	1.943	1.218	×
.600	2.175	1.364	×
.720	2.290	1.436	×
.840	2.406	1.508	×
1.080	2.638	1.654	×
1.200	2.754	1.727	×

Table I. Concluded

(i) Lower flap surface for 15° vectored primary flow;
NS 1.595 to NS 3.049 (see fig. 5(e))

x', in.	x, in.	x/x_t	y, in.
			0
0.120	1.711	1.073	×
.240	1.827	1.145	×
.360	1.943	1.218	×
.480	2.059	1.291	×
.720	2.291	1.436	×
.840	2.406	1.508	×
.960	2.522	1.581	×
1.080	2.638	1.654	×
1.200	2.754	1.727	×

Table II. Internal-Static Pressure Ratios

(a) Sidewall surface for 0° vectored nozzle

$w/w_t = 0$

	$p/p_{t,j}$ for x/x_t of —											
NPR	.404	.498	.624	.749	.875	.937	1.122	1.216	1.373	1.530	1.687	1.843
1.001	.999	1.001	1.000	1.000	1.000	1.000	1.000	1.000	1.000	1.000	1.000	1.000
2.002	.965	.964	.963	.954	.913	.856	.385	.393	.420	.437	.456	.500
2.496	.964	.962	.963	.954	.913	.856	.388	.391	.416	.432	.441	.453
3.015	.964	.963	.963	.954	.913	.856	.387	.385	.410	.427	.438	.451
3.500	.965	.965	.963	.954	.913	.856	.390	.384	.409	.424	.439	.453
3.997	.965	.966	.964	.953	.914	.856	.391	.382	.408	.425	.441	.457

$w/w_t = 0.095$

	$p/p_{t,j}$ for x/x_t of —									
NPR	.561	.624	.749	.843	.937	1.063	1.157	1.313	1.470	1.627
1.001	1.001	1.001	1.000	1.000	1.000	1.002	1.000	1.000	1.000	1.000
2.002	.960	.960	.930	.930	.850	.487	.401	.402	.441	.443
2.496	.961	.961	.930	.930	.850	.490	.400	.397	.444	.438
3.015	.962	.962	.930	.930	.850	.490	.398	.393	.443	.434
3.500	.964	.963	.932	.932	.850	.491	.399	.392	.445	.432
3.997	.965	.963	.933	.933	.851	.491	.398	.393	.447	.433

$w/w_t = 0.219$

	$p/p_{t,j}$ for x/x_t of —			
NPR	.561	.624	.749	.843
1.001	1.001	1.001	1.000	1.001
2.002	.968	.964	.956	.933
2.496	.967	.965	.957	.935
3.015	.967	.965	.959	.936
3.500	.968	.967	.961	.936
3.997	.968	.967	.963	.937

Table II. Continued

(a) Continued

$w/w_t = 0.343$

NPR	$p/p_{t,j}$ for x/x_t of —					
	.404	.498	.561	.624	.749	.843
1.001	1.001	1.001	1.001	1.001	1.002	1.049
2.002	.964	.967	.969	.969	.966	.971
2.496	.963	.966	.968	.970	.964	.967
3.015	.964	.967	.969	.972	.967	.966
3.500	.964	.968	.971	.973	.968	.963
3.997	.965	.968	.972	.975	.968	.963

$w/w_t = 0.467$

NPR	$p/p_{t,j}$ for x/x_t of —				
	.404	.498	.561	.624	.749
1.001	1.000	1.000	1.002	.999	1.002
2.002	.963	.969	.970	.976	.969
2.496	.962	.969	.971	.976	.968
3.015	.962	.968	.973	.976	.968
3.500	.963	.969	.974	.978	.969
3.997	.964	.971	.976	.978	.970

$w/w_t = 0.590$

NPR	$p/p_{t,j}$ for x/x_t of —			
	.373	.404	.498	.561
1.001	1.000	1.001	1.001	1.000
2.002	.955	.963	.970	.974
2.496	.954	.961	.969	.975
3.015	.955	.962	.970	.976
3.500	.957	.963	.971	.976
3.997	.958	.963	.971	.977

Table II. Continued

(a) Concluded

$w/w_t = 0.714$

NPR	$p/p_{t,j}$ for x/x_t of —				
	.373	.404	.498	.561	.624
1.001	1.001	1.000	1.000	1.001	1.000
2.002	.949	.953	.963	.971	.968
2.496	.949	.951	.962	.971	.967
3.015	.949	.951	.963	.973	.967
3.500	.949	.952	.963	.974	.967
3.997	.950	.952	.964	.975	.967

$w/w_t = 0.838$

NPR	$p/p_{t,j}$ for x/x_t of —			
	.373	.404	.498	.624
1.001	1.001	1.000	1.001	1.000
2.002	.928	.934	.954	.955
2.496	.924	.930	.951	.952
3.015	.924	.930	.952	.951
3.500	.925	.931	.952	.949
3.997	.925	.931	.952	.949

$w/w_t = 0.933$

NPR	$p/p_{t,j}$ for x/x_t of —		
	.498	.561	.624
1.001	1.001	1.000	1.000
2.002	.934	.945	.942
2.496	.933	.943	.939
3.015	.932	.942	.937
3.500	.932	.943	.938
3.997	.932	.943	.937

$w/w_t = 1.029$

NPR	$p/p_{t,j}$ for x/x_t of —		
	.498	.561	.624
1.001	1.000	1.001	1.001
2.002	.904	.924	.933
2.496	.899	.921	.929
3.015	.898	.921	.928
3.500	.898	.921	.929
3.997	.897	.920	.928

Table II. Continued

(b) Sidewall surface for 15° vectored nozzle

$w/w_t = 0$

NPR	$p/p_{t,j}$ for x/x_t of —					
	.404	.498	.624	.749	.875	.937
1.000	.999	1.001	1.000	1.003	1.000	1.000
2.006	.969	.966	.967	.959	.926	.882
2.505	.967	.966	.966	.958	.926	.881
3.006	.968	.967	.966	.958	.926	.881
3.514	.968	.968	.966	.958	.926	.881
4.011	.968	.969	.967	.958	.926	.881

$\eta/\eta_t = 0$

$p/p_{t,j}$ for x/x_t of —					
1.061	1.151	1.302	1.454	1.605	1.758
.999	1.000	1.000	1.003	.999	1.000
.656	.463	.406	.389	.416	.443
.656	.464	.404	.387	.414	.433
.655	.465	.402	.385	.412	.434
.655	.466	.400	.383	.413	.437
.656	.467	.398	.383	.414	.440

$w/w_t = 0.095$

NPR	$p/p_{t,j}$ for x/x_t of —				
	.561	.624	.749	.843	.937
1.000	.999	1.001	.999	.999	1.000
2.006	.965	.966	.941	.941	.879
2.505	.965	.966	.940	.940	.878
3.006	.965	.966	.940	.940	.878
3.514	.966	.967	.942	.942	.878
4.011	.967	.968	.943	.943	.879

$\eta/\eta_t = 0.452$

$p/p_{t,j}$ for x/x_t of —				
1.045	1.134	1.286	1.437	1.589
1.001	1.002	1.001	1.000	1.000
.565	.378	.448	.378	.434
.566	.381	.447	.380	.436
.565	.379	.446	.381	.436
.564	.379	.446	.380	.435
.564	.386	.446	.382	.435

$w/w_t = 0.219$

NPR	$p/p_{t,j}$ for x/x_t of —			
	.561	.624	.749	.843
1.000	1.001	.998	1.000	1.000
2.006	.972	.968	.962	.942
2.505	.970	.968	.962	.942
3.006	.971	.969	.963	.943
3.514	.970	.970	.965	.943
4.011	.971	.971	.967	.944

Table II. Continued

(b) Continued

$w/w_t = 0.343$

NPR	$p/p_{t,j}$ for x/x_t of —				
	.404	.498	.561	.624	.749
1.000	.998	1.000	.999	1.003	1.000
2.006	.968	.971	.974	.975	.971
2.505	.966	.969	.973	.976	.969
3.006	.966	.971	.973	.977	.971
3.514	.967	.971	.975	.976	.971
4.011	.968	.972	.975	.976	.972

$w/w_t = 0.467$

NPR	$p/p_{t,j}$ for x/x_t of —				
	.404	.498	.561	.624	.749
1.000	.998	1.000	1.000	.997	.999
2.006	.968	.971	.974	.979	.974
2.505	.966	.972	.974	.979	.972
3.006	.966	.971	.975	.980	.972
3.514	.967	.971	.976	.981	.973
4.011	.967	.974	.978	.981	.973

$w/w_t = 0.590$

NPR	$p/p_{t,j}$ for x/x_t of —			
	.373	.404	.498	.561
1.000	1.000	1.000	.999	.998
2.006	.960	.965	.974	.978
2.505	.957	.963	.972	.977
3.006	.958	.964	.972	.978
3.514	.959	.965	.973	.978
4.011	.961	.965	.974	.979

Table II. Continued

(b) Concluded

$w/w_t = 0.714$

NPR	$p/p_{t,j}$ for x/x_t of —				
	.373	.404	.498	.561	.624
1.000	.999	.999	.998	1.000	.999
2.006	.954	.957	.967	.976	.972
2.505	.953	.955	.966	.976	.970
3.006	.953	.955	.966	.977	.970
3.514	.953	.955	.966	.977	.970
4.011	.953	.955	.967	.978	.970

$w/w_t = 0.838$

NPR	$p/p_{t,j}$ for x/x_t of —			
	.373	.404	.498	.624
1.000	1.000	1.000	1.000	1.000
2.006	.933	.941	.960	.959
2.505	.930	.937	.956	.956
3.006	.929	.936	.956	.955
3.514	.930	.936	.956	.953
4.011	.930	.936	.956	.953

$w/w_t = 0.933$

NPR	$p/p_{t,j}$ for x/x_t of —		
	.498	.561	.624
1.000	1.001	1.000	1.000
2.006	.942	.950	.948
2.505	.940	.948	.944
3.006	.940	.947	.943
3.514	.939	.948	.943
4.011	.940	.948	.943

$w/w_t = 1.029$

NPR	$p/p_{t,j}$ for x/x_t of —		
	.498	.561	.624
1.000	.999	1.001	.999
2.006	.914	.933	.941
2.505	.909	.928	.937
3.006	.908	.930	.936
3.514	.908	.929	.936
4.011	.908	.928	.936

Table II. Continued

(c) Upper flap surface for 0° vectored nozzle

NPR	$p/p_{t,j}$ for x/x_t of —							
	.694	.700	.705	.762	.809	.854	.903	.948
1.000	1.004	.998	.999	.998	.999	1.001	1.000	1.001
2.027	.952	.974	.986	1.005	.996	.985	.969	.934
2.504	.950	.973	.987	1.006	.999	.985	.971	.935
3.026	.949	.972	.987	1.007	.999	.987	.971	.935
3.511	.947	.974	.989	1.009	1.002	.990	.973	.937
4.003	.948	.973	.990	1.009	1.003	.991	.973	.937

NPR	$p/p_{t,j}$ for x/x_t of —						
	1.076	1.149	1.224	1.452	1.527	1.678	1.753
1.000	1.000	1.000	1.001	1.000	1.001	.999	1.000
2.027	.359	.454	.377	.362	.346	.366	.420
2.504	.356	.456	.382	.366	.337	.367	.420
3.026	.351	.457	.381	.367	.331	.367	.418
3.511	.351	.459	.383	.370	.331	.368	.417
4.003	.349	.461	.385	.372	.332	.370	.415

Table II. Concluded

(d) Upper flap surface for 15° vectored nozzle

NPR	$p/p_{t,j}$ for x/x_t of —							
	.694	.705	.762	.809	.854	.903	.948	1.072
1.000	1.001	1.001	1.001	1.001	1.000	1.001	1.000	1.000
2.001	.969	.989	1.004	1.003	.991	.976	.946	.710
2.516	.966	.987	1.005	1.002	.991	.975	.945	.710
3.011	.964	.985	1.005	1.001	.992	.973	.944	.710
3.500	.966	.986	1.007	1.002	.993	.977	.945	.711
3.999	.966	.986	1.007	1.002	.993	.978	.944	.710

NPR	$p/p_{t,j}$ for x/x_t of —						
	1.145	1.219	1.366	1.437	1.510	1.653	1.727
1.000	1.000	1.000	1.000	.999	1.000	1.001	1.000
2.001	.611	.490	.294	.241	.415	.456	.362
2.516	.609	.489	.291	.232	.413	.393	.363
3.011	.610	.491	.297	.238	.415	.394	.365
3.500	.612	.492	.299	.239	.418	.395	.367
3.999	.612	.493	.299	.239	.419	.395	.367

(e) Lower flap surface for 15° vectored nozzle

NPR	$p/p_{t,j}$ for x/x_t of —								
	1.072	1.145	1.219	1.296	1.437	1.510	1.584	1.653	1.727
1.000	1.000	1.000	1.010	1.000	1.000	1.000	1.000	.999	1.000
2.001	.418	.428	.325	.324	.366	.448	.444	.354	.240
2.516	.417	.427	.307	.320	.364	.448	.441	.345	.231
3.011	.420	.431	.307	.323	.367	.449	.442	.345	.239
3.500	.421	.434	.304	.325	.369	.452	.443	.344	.239
3.999	.423	.435	.304	.325	.369	.453	.444	.343	.238

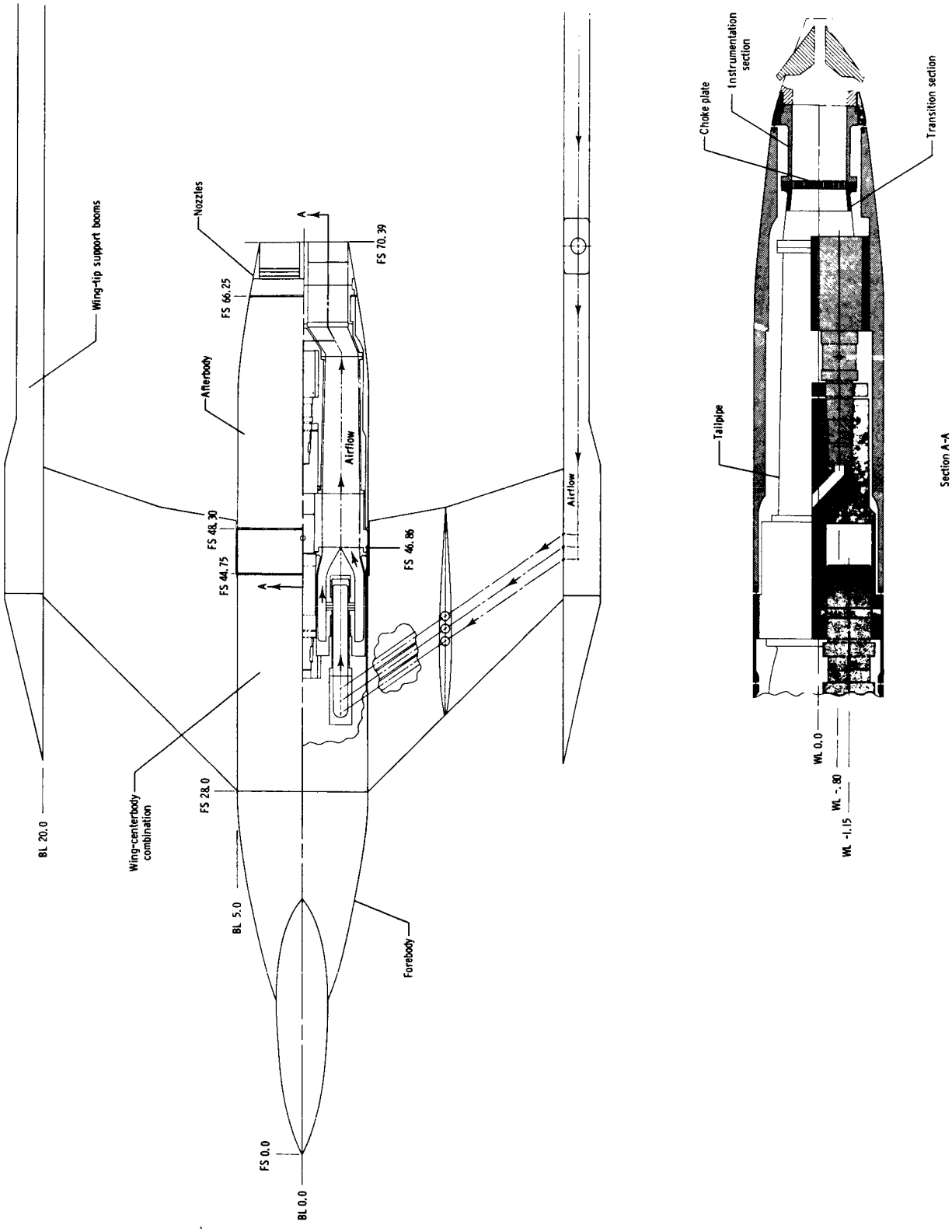

Figure 1. Wing-tip-supported model with 50-percent-deployed, 0° vectored nozzle showing jet simulation system. All linear dimensions are in inches.

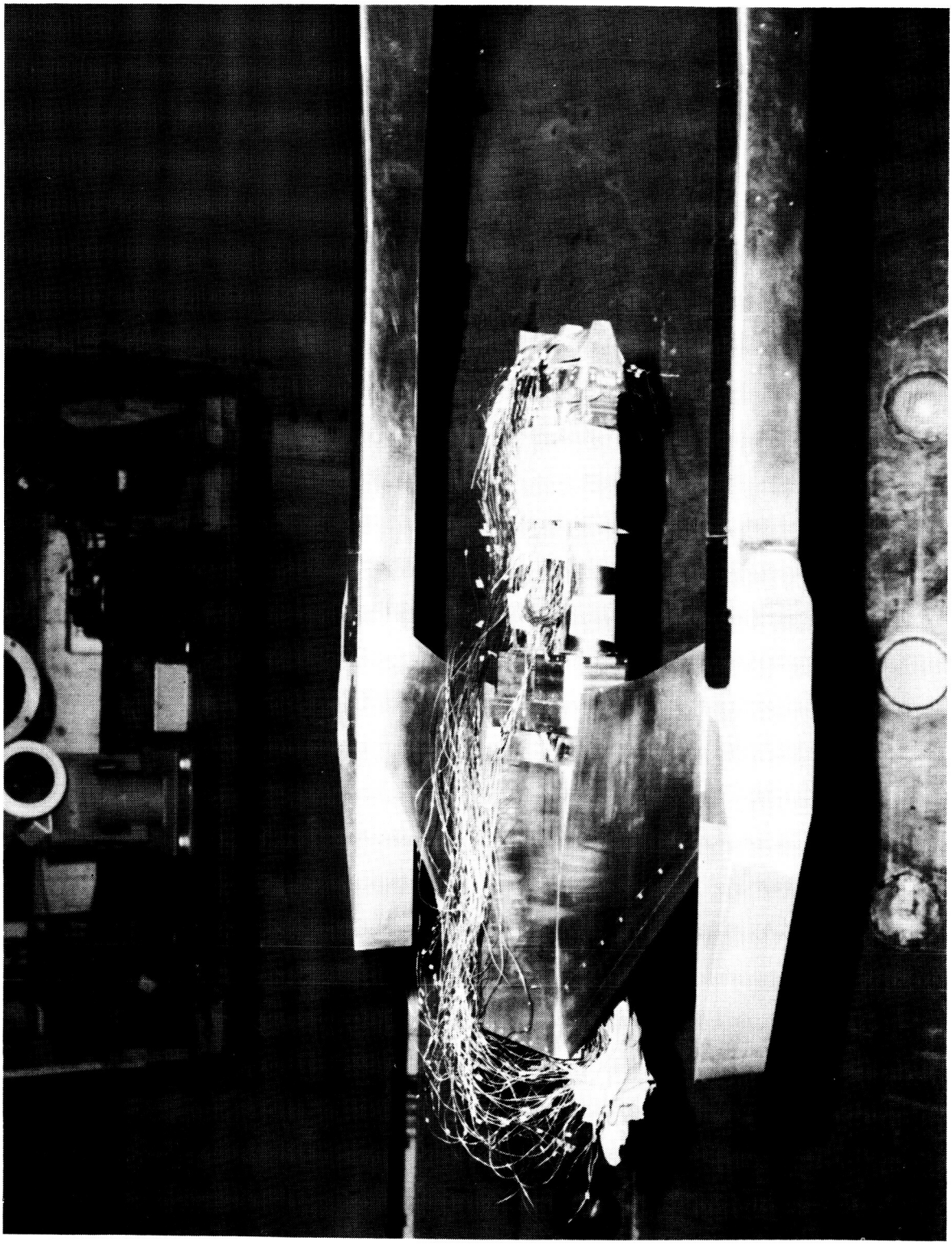

L-85-759

Figure 2. Overall view of test setup.

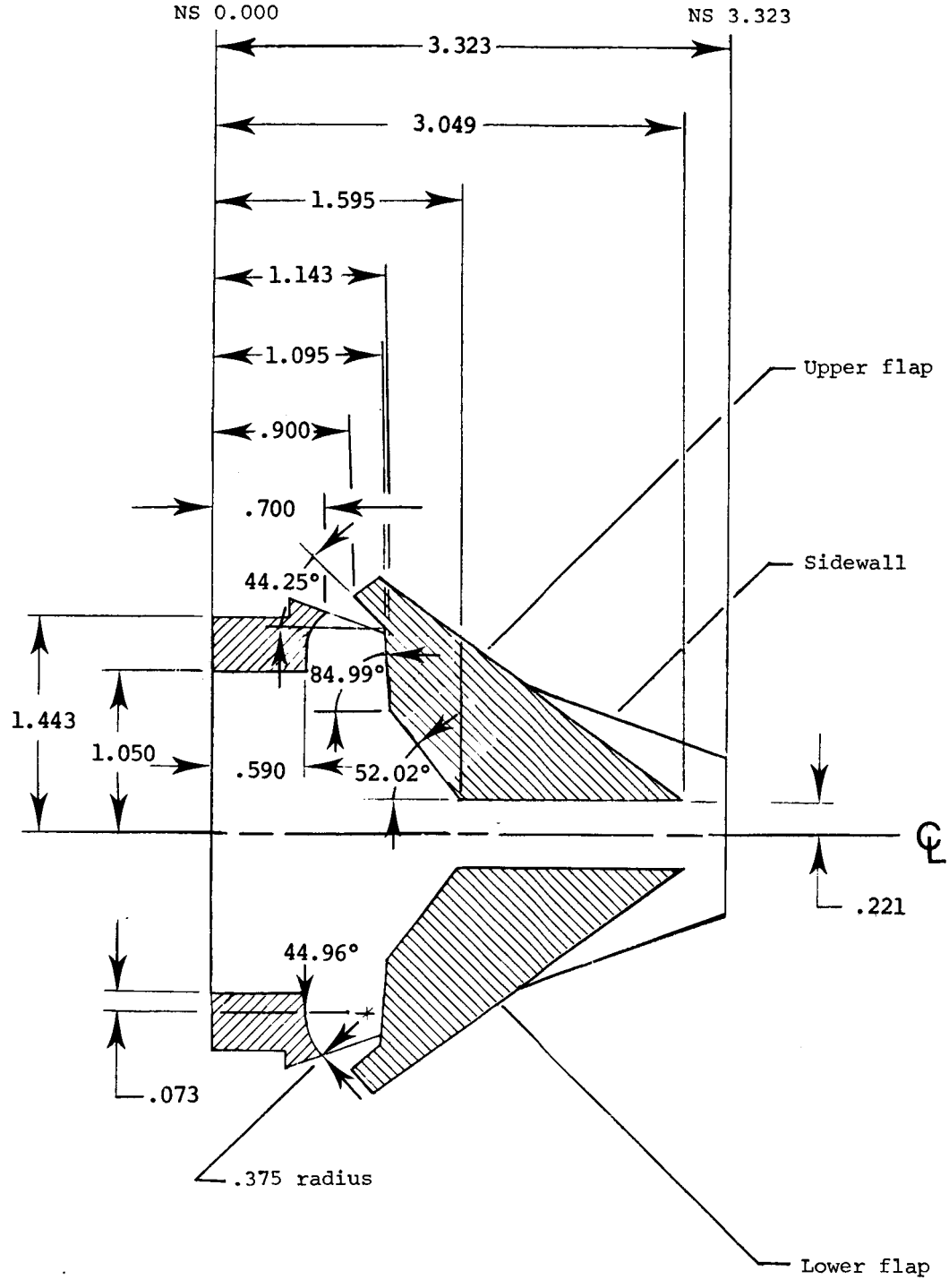

(a) 0° vectored primary flow.

Figure 3. Geometric details of nozzle with reverser deployed 50 percent. All linear dimensions are in inches.

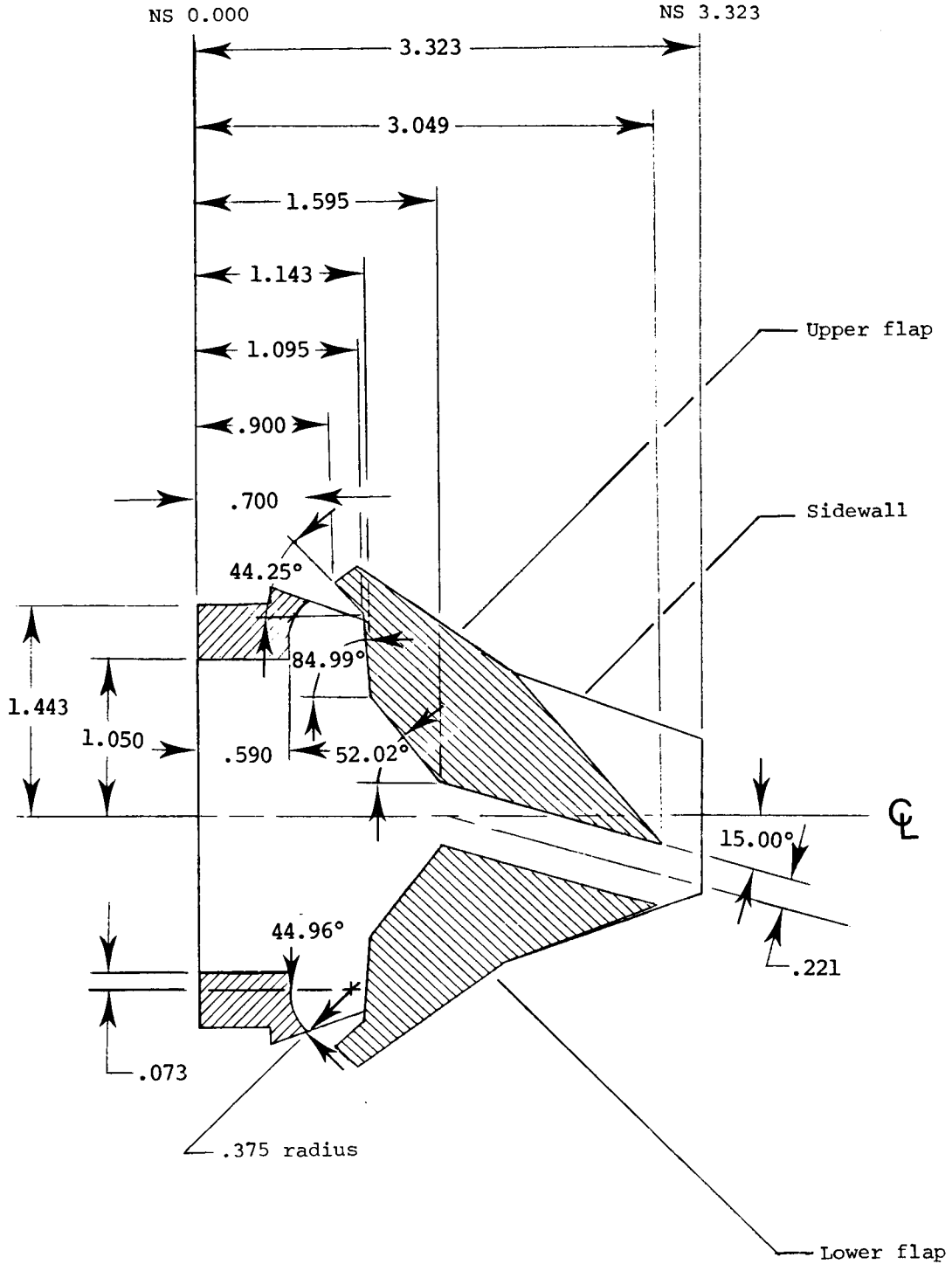

(b) 15° vectored primary flow.

Figure 3. Concluded.

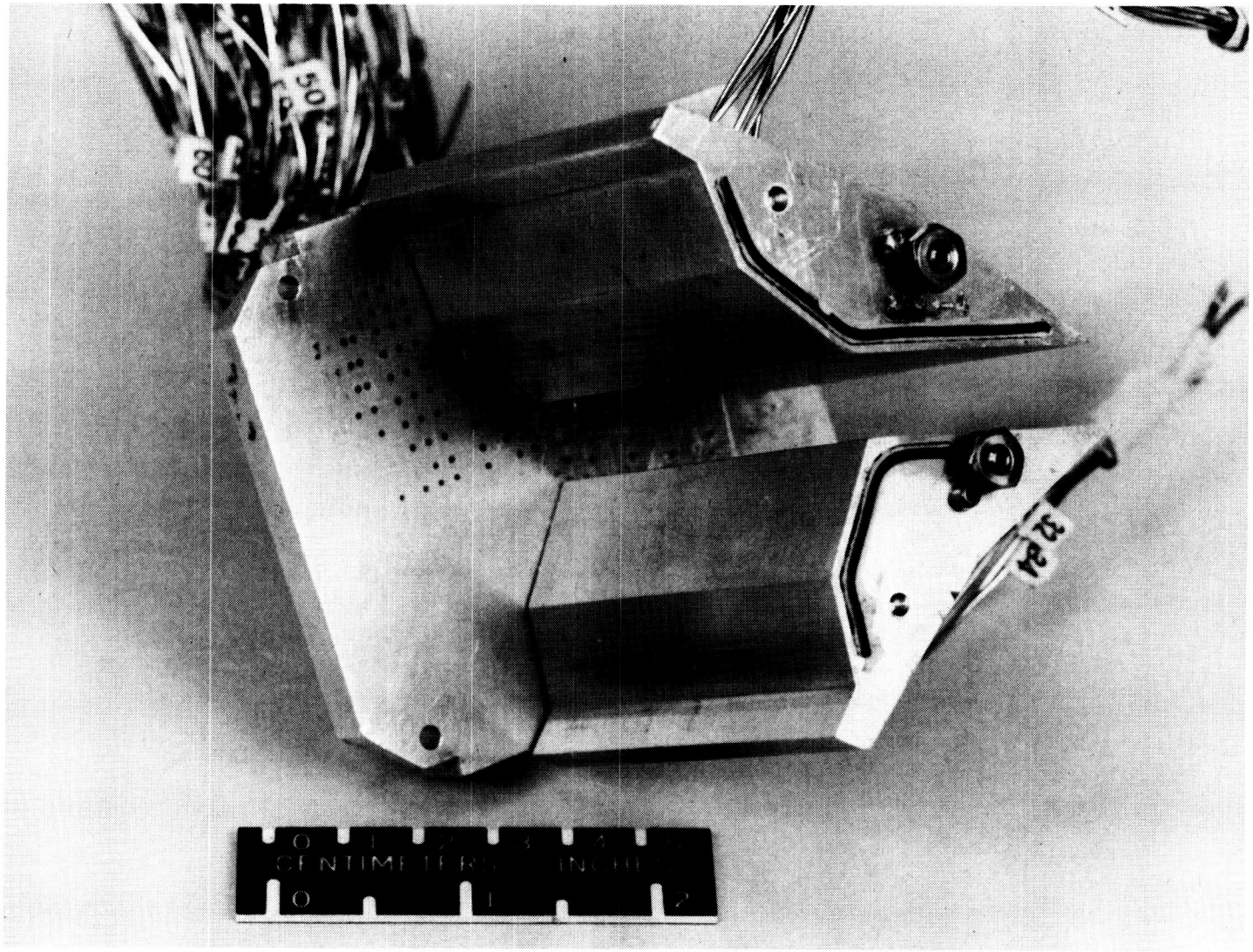

L-85-12,986

(a) Quarter view of right nozzle with left sidewall removed.

Figure 4. Nozzle configuration with thrust reverser deployed 50 percent and primary flow vectored 15°.

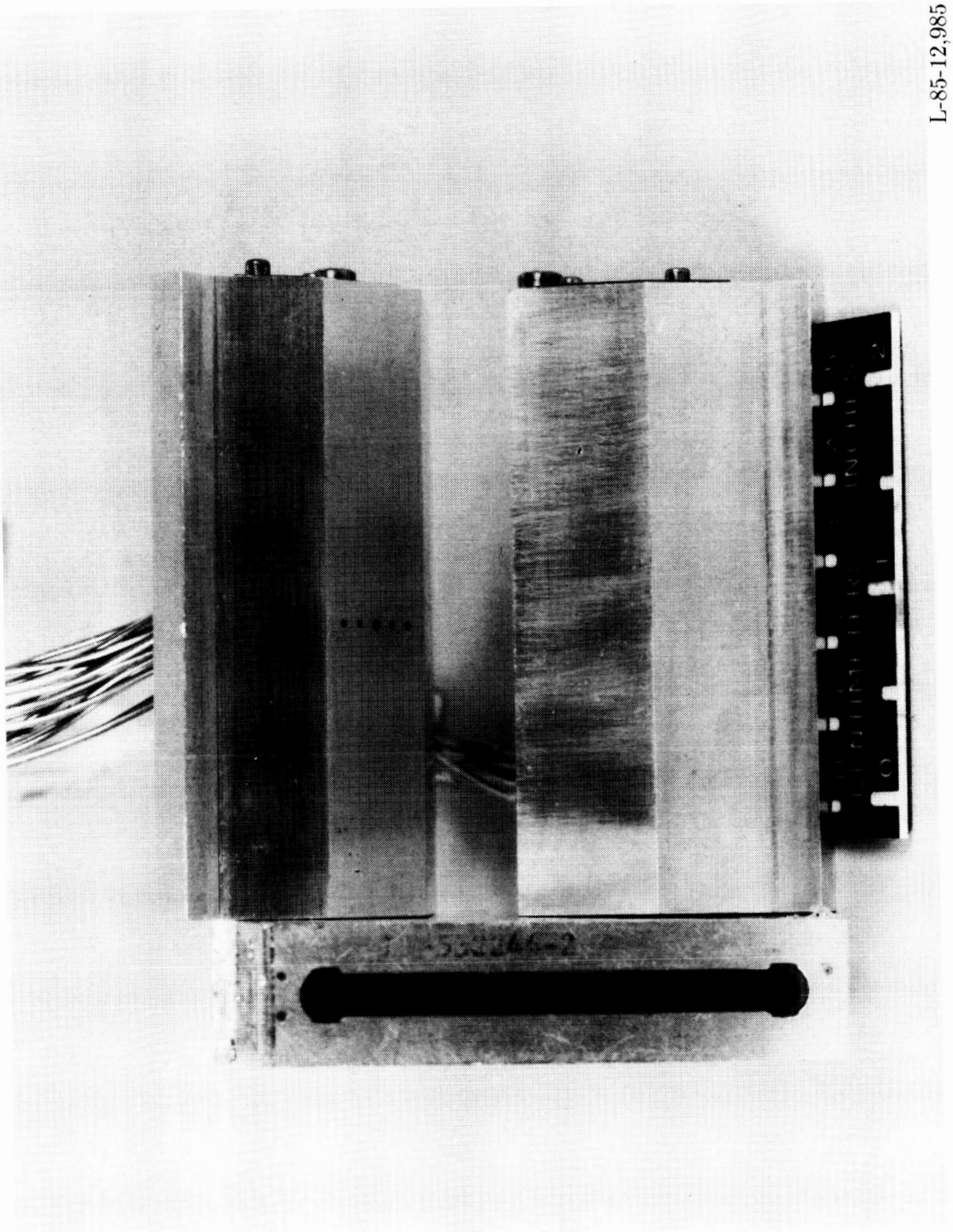

L-85-12,985

(b) Front view of left nozzle with left sidewall removed.

Figure 4. Concluded.

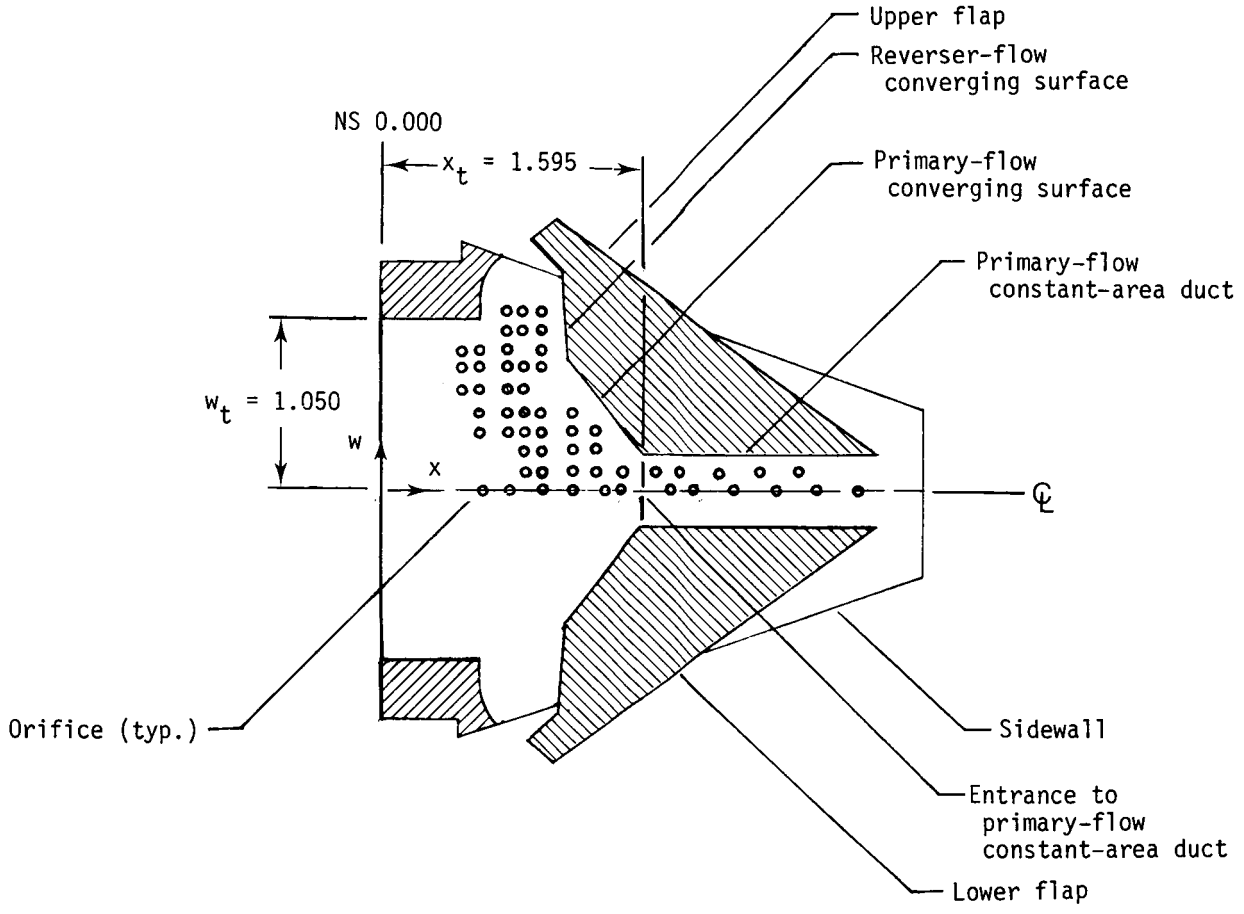

(a) 0° vectored primary flow.

Figure 5. Internal static-pressure orifices of nozzle with reverser deployed 50 percent. Orifice locations are given in table I. All linear dimensions are in inches.

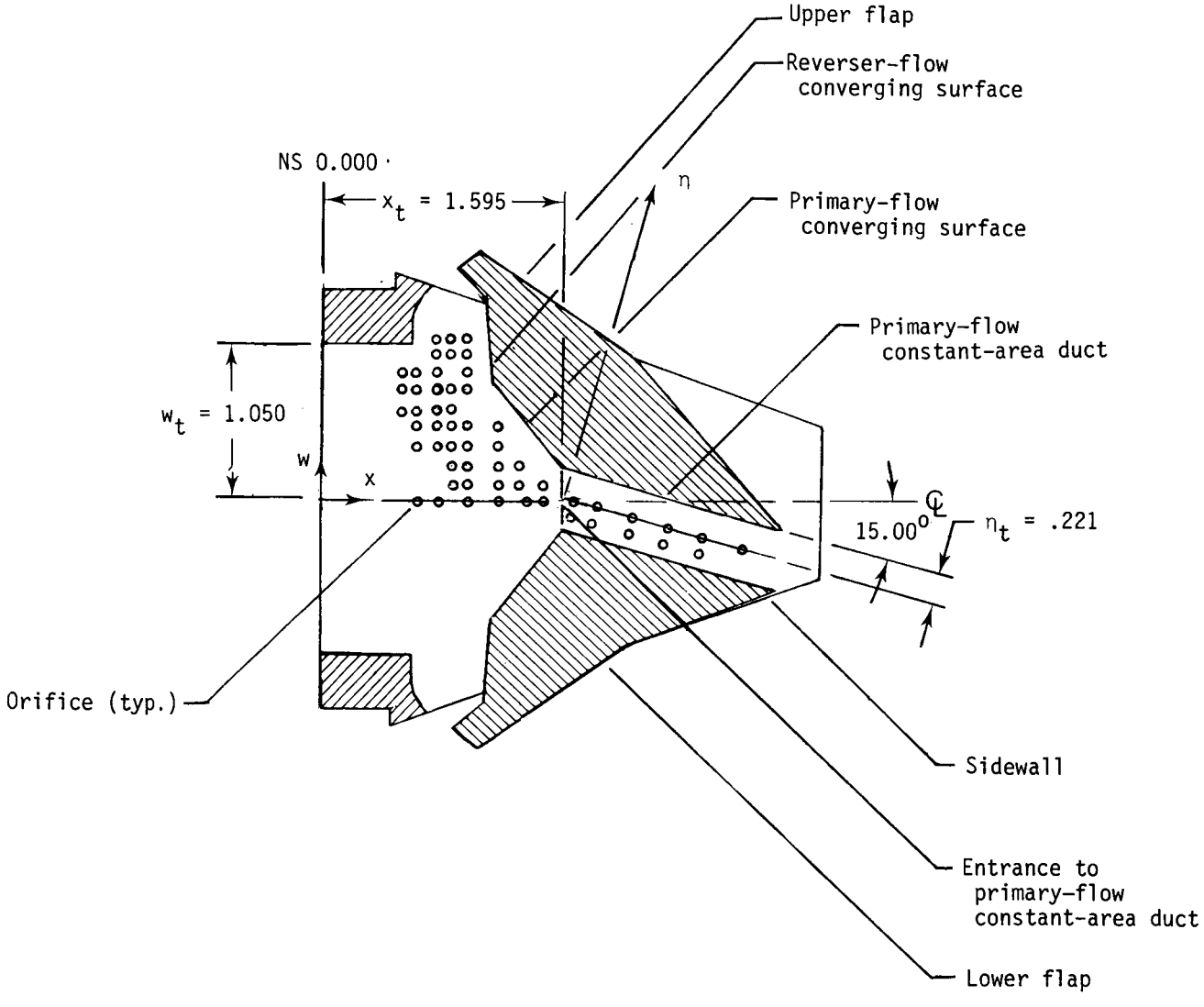

(b) 15° vectored primary flow.

Figure 5. Continued.

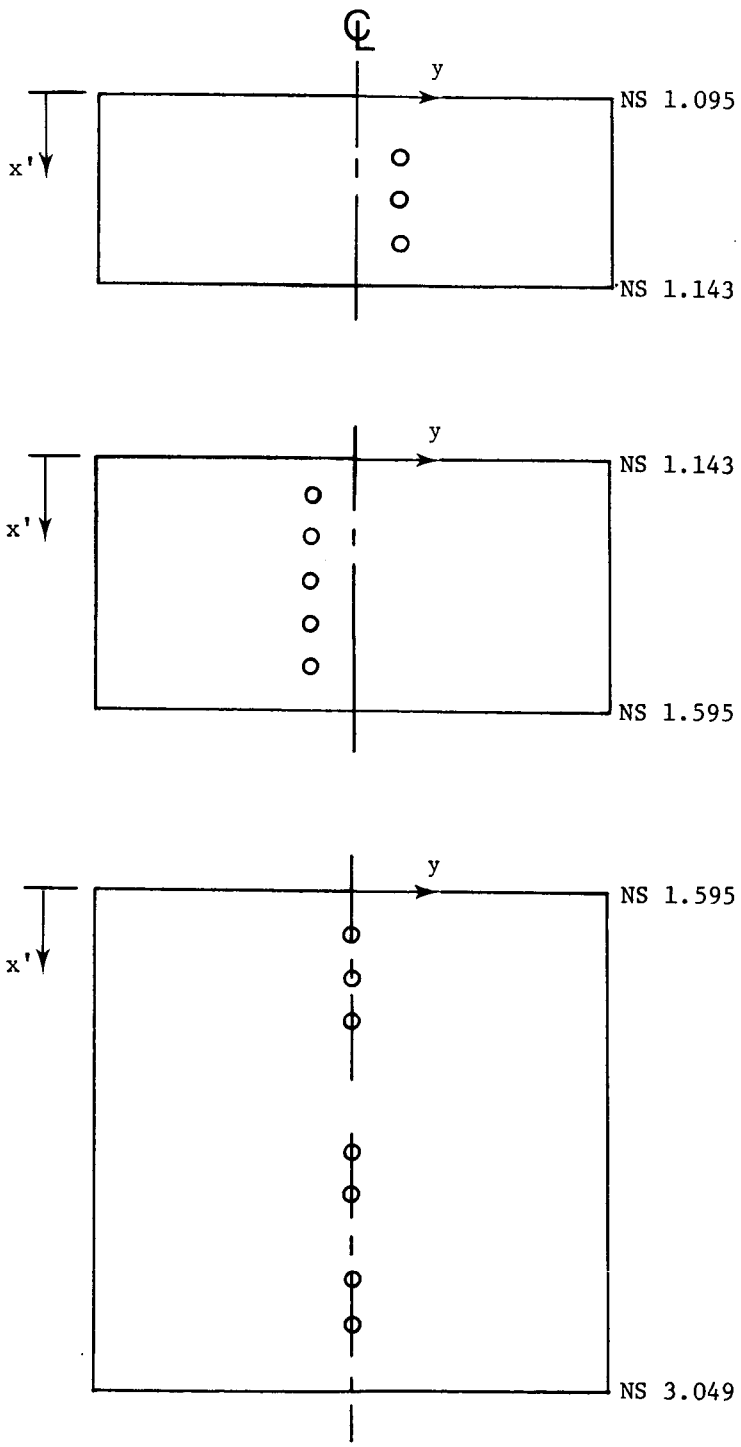

(c) Internal surface of 0° vectored upper flap (see fig. 3(a)).

Figure 5. Continued.

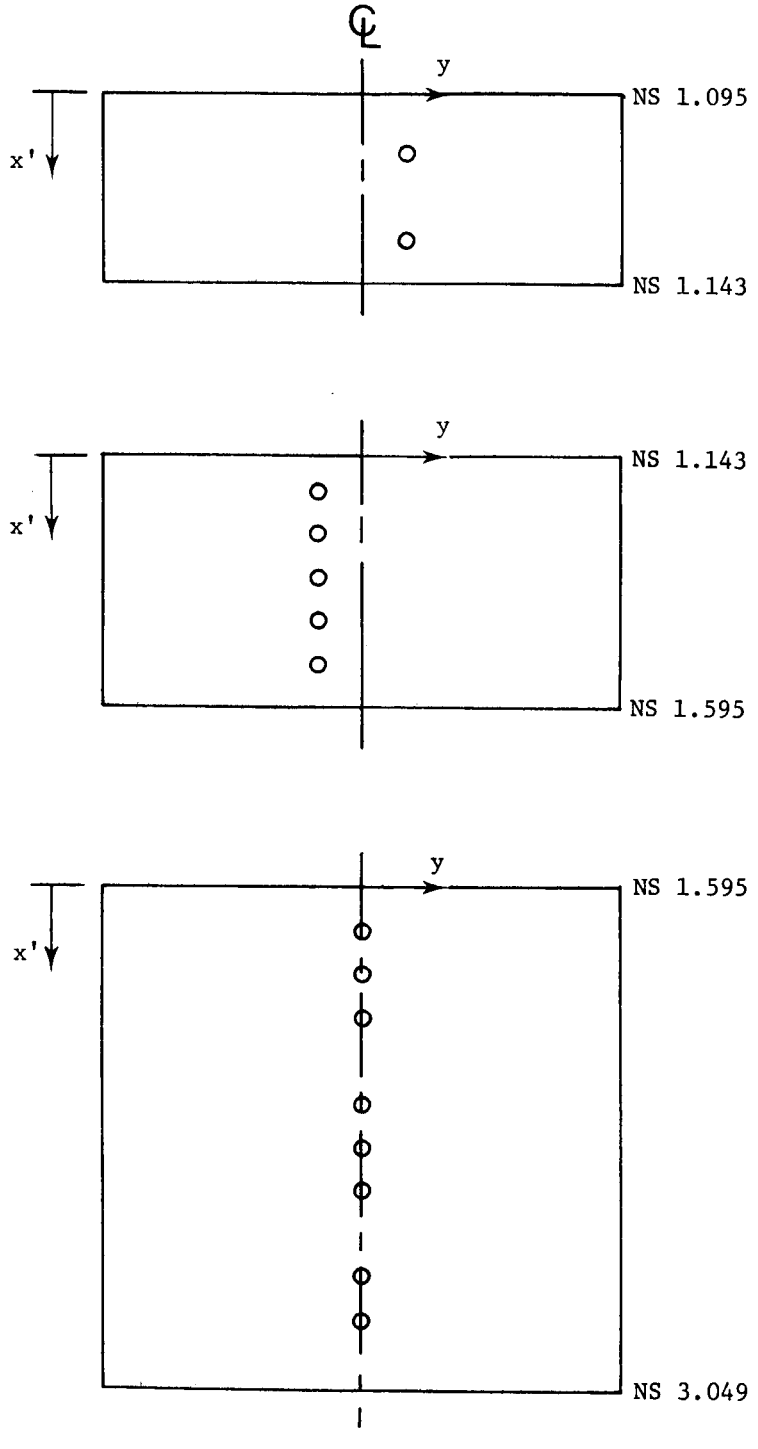

(d) Internal surface of 15° vectored upper flap (see fig. 3(b)).

Figure 5. Continued.

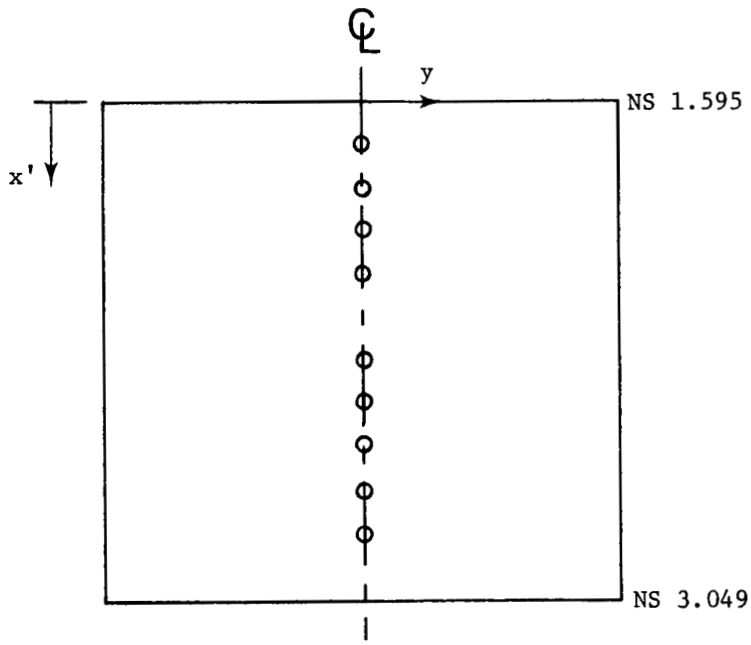

(e) Internal surface of 15° vectored lower flap (see fig. 3(b)).

Figure 5. Concluded.

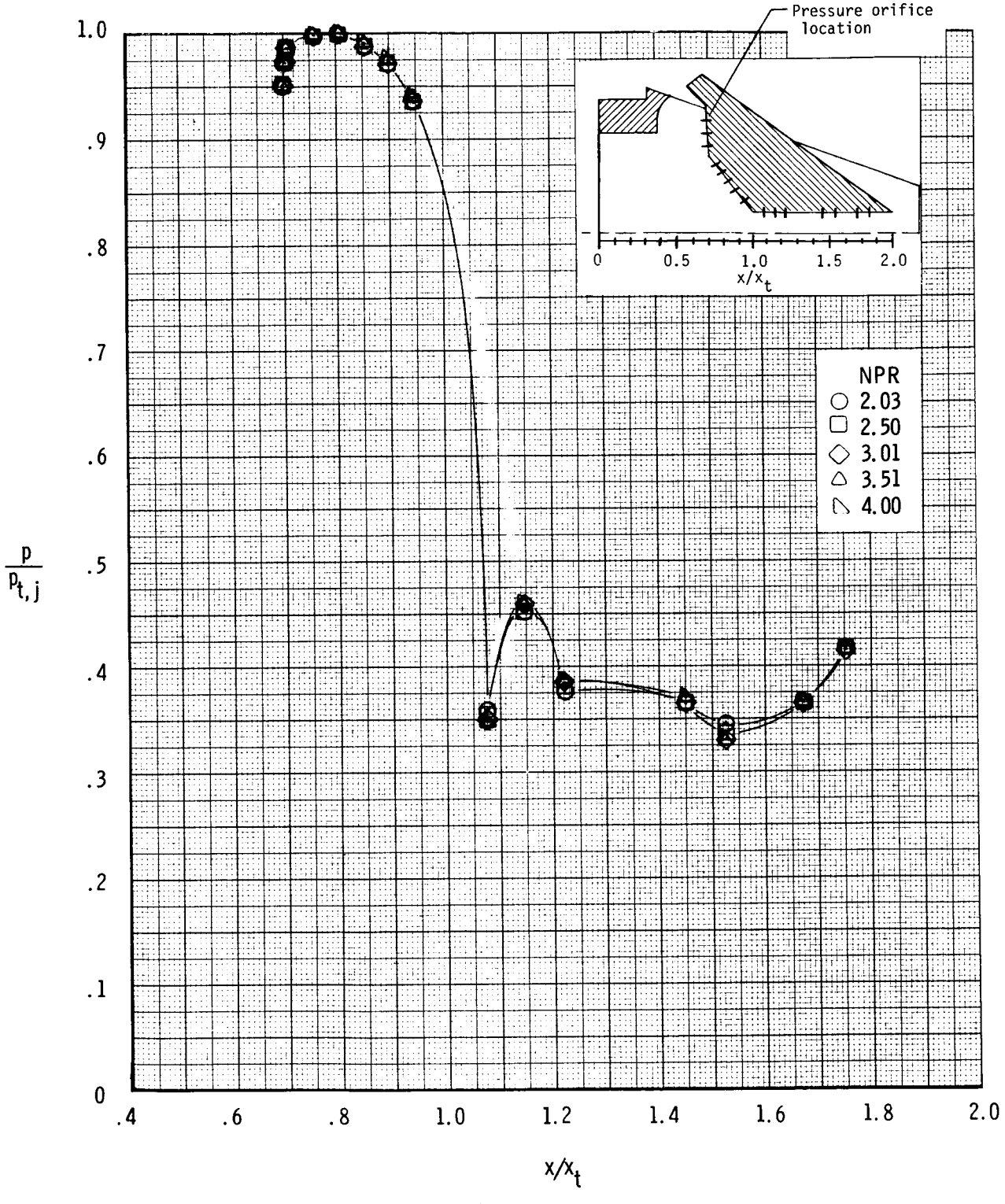

(a) Upper flap centerline pressures.

Figure 6. Nozzle pressure distribution for 0° vectored configuration.

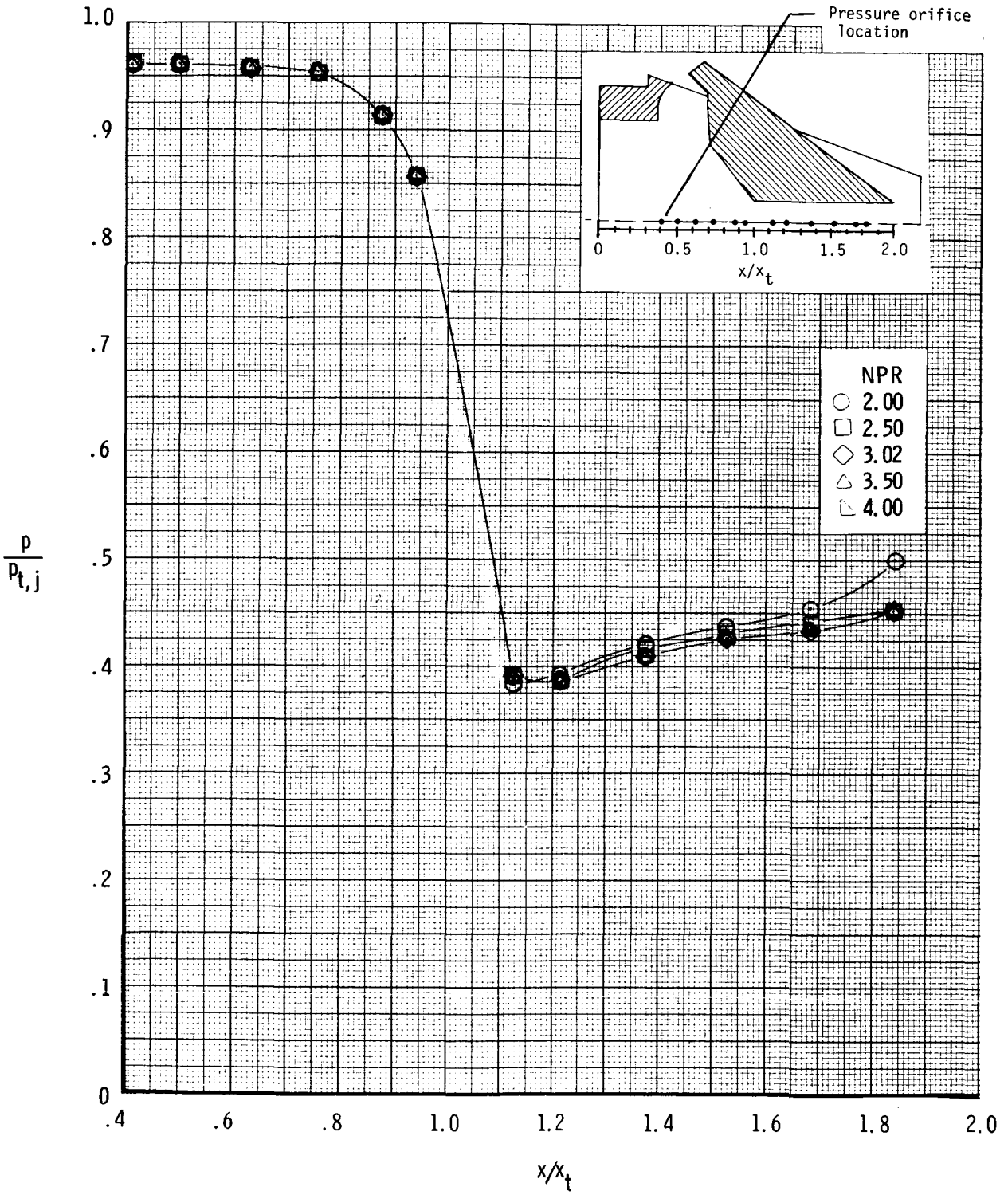

(b) Sidewall centerline pressures; $w/w_t = 0$.
Figure 6. Continued.

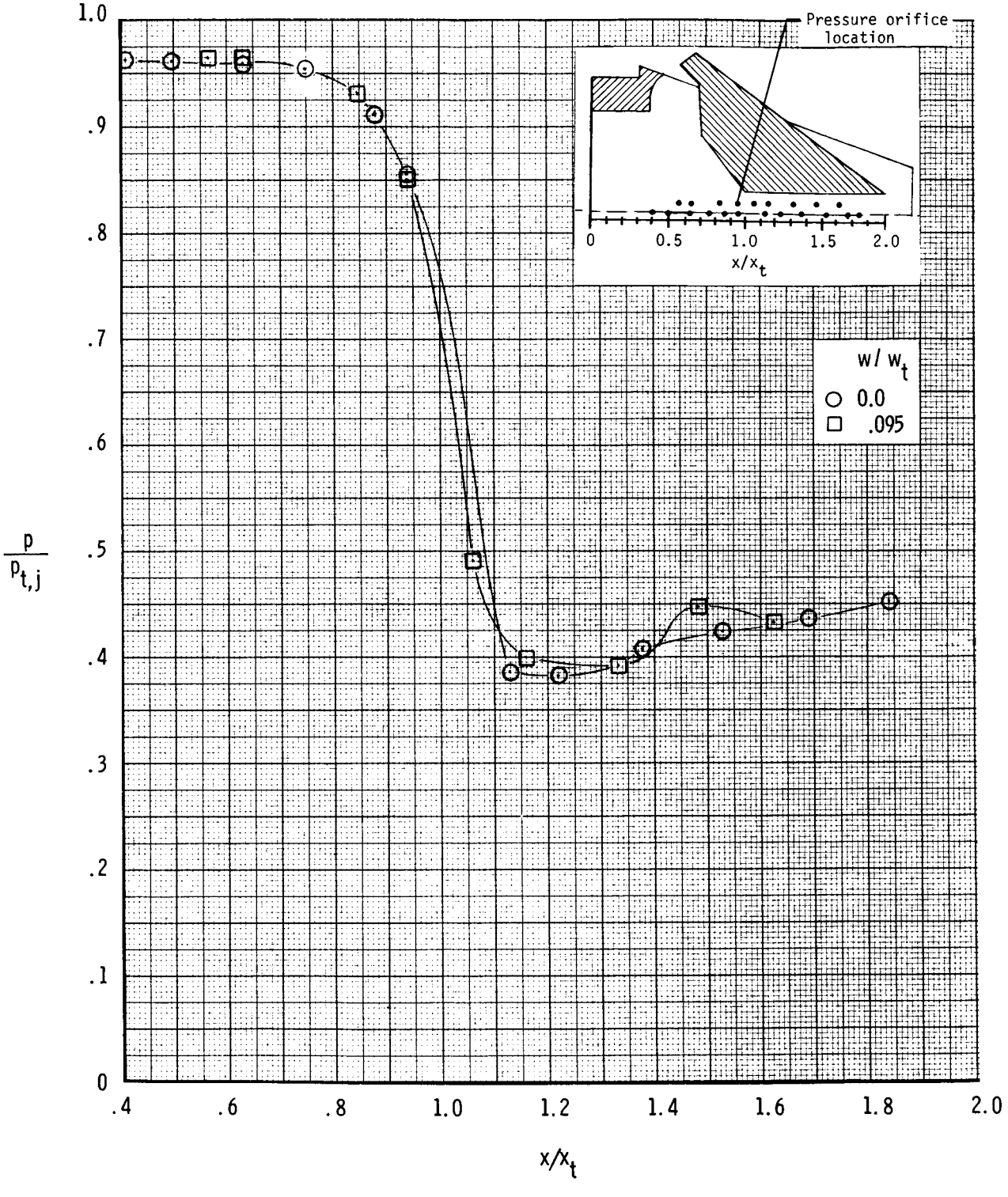

(c) Variation of pressure across nozzle sidewall at NPR = 4.0.
Figure 6. Continued.

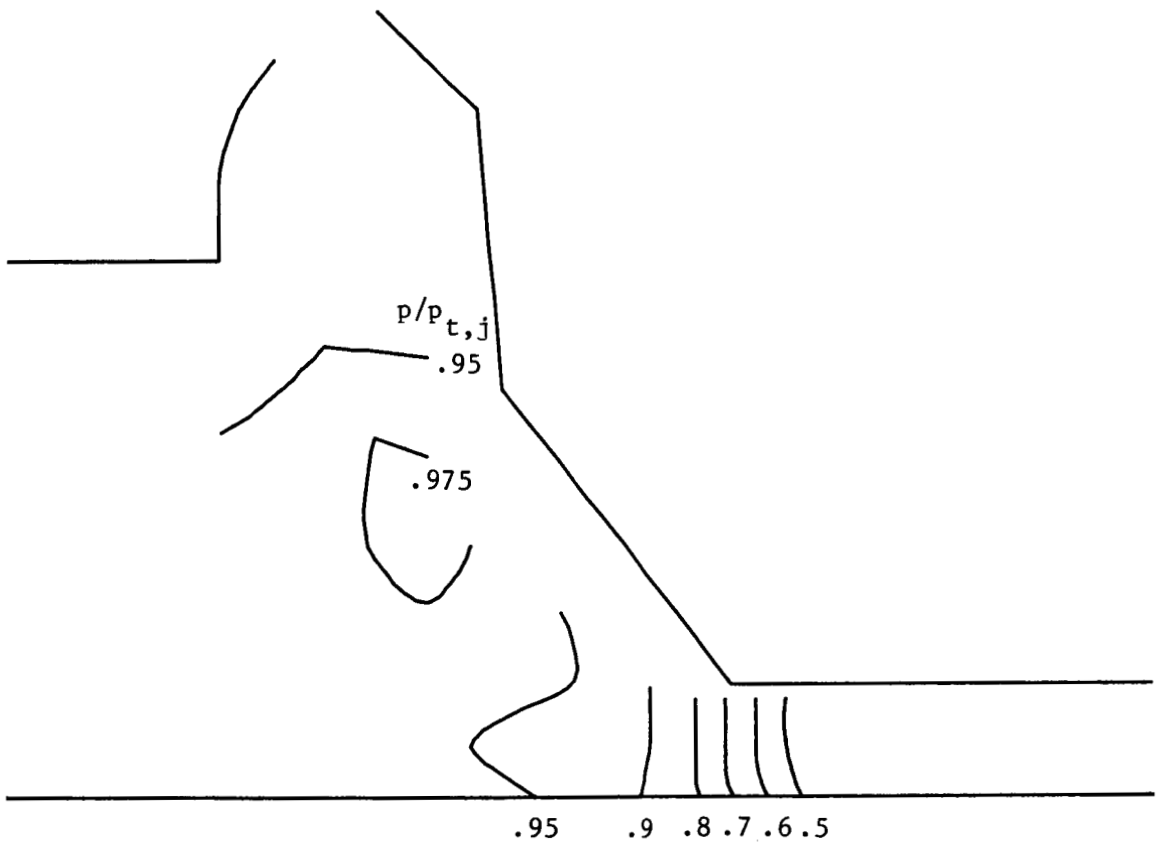

(d) Contours of $p/p_{t,j}$ on 0° vectored nozzle sidewall for NPR = 4.0.

Figure 6. Concluded.

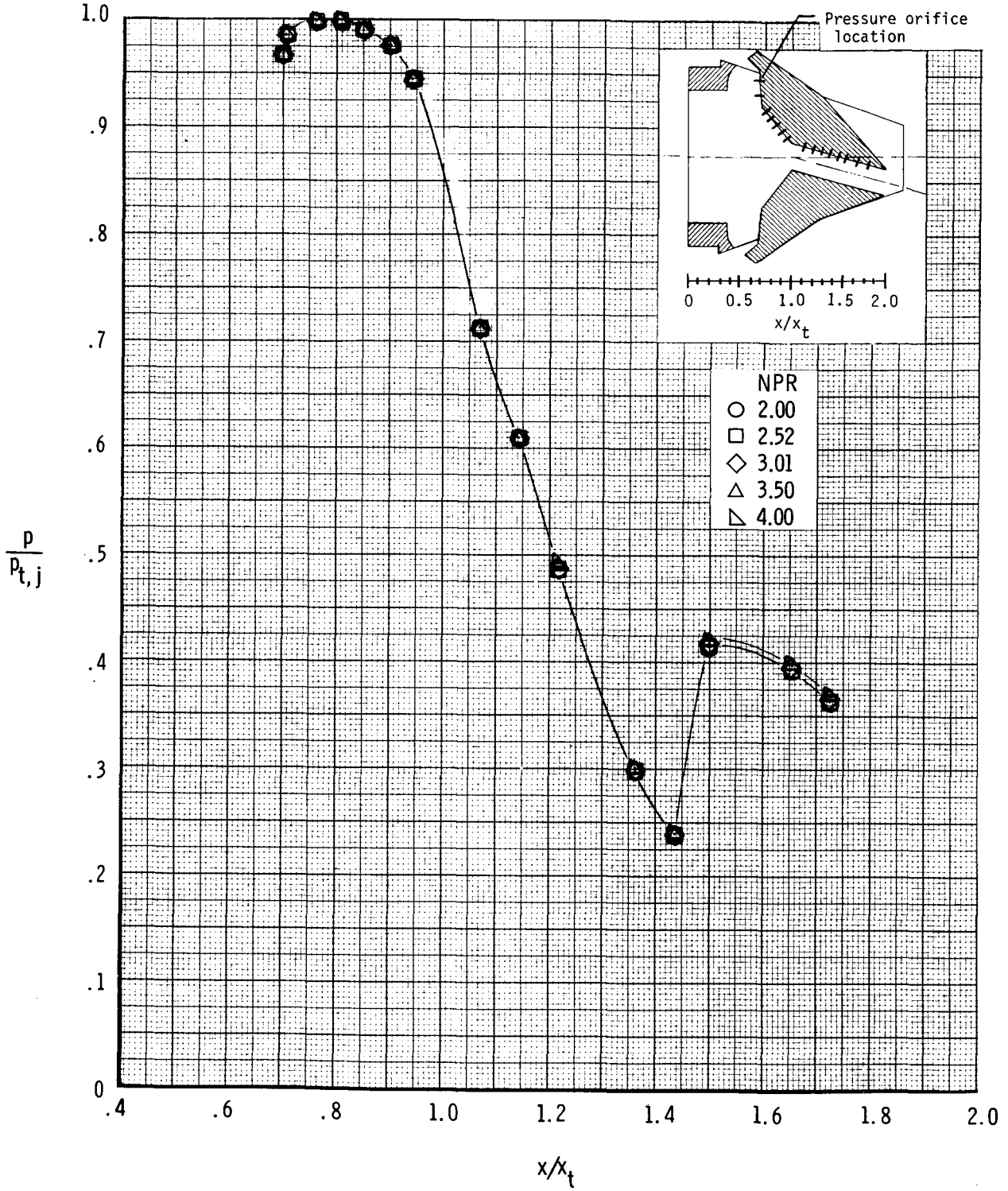

(a) Upper flap centerline pressures.

Figure 7. Nozzle pressure distribution for 15° vectored configuration.

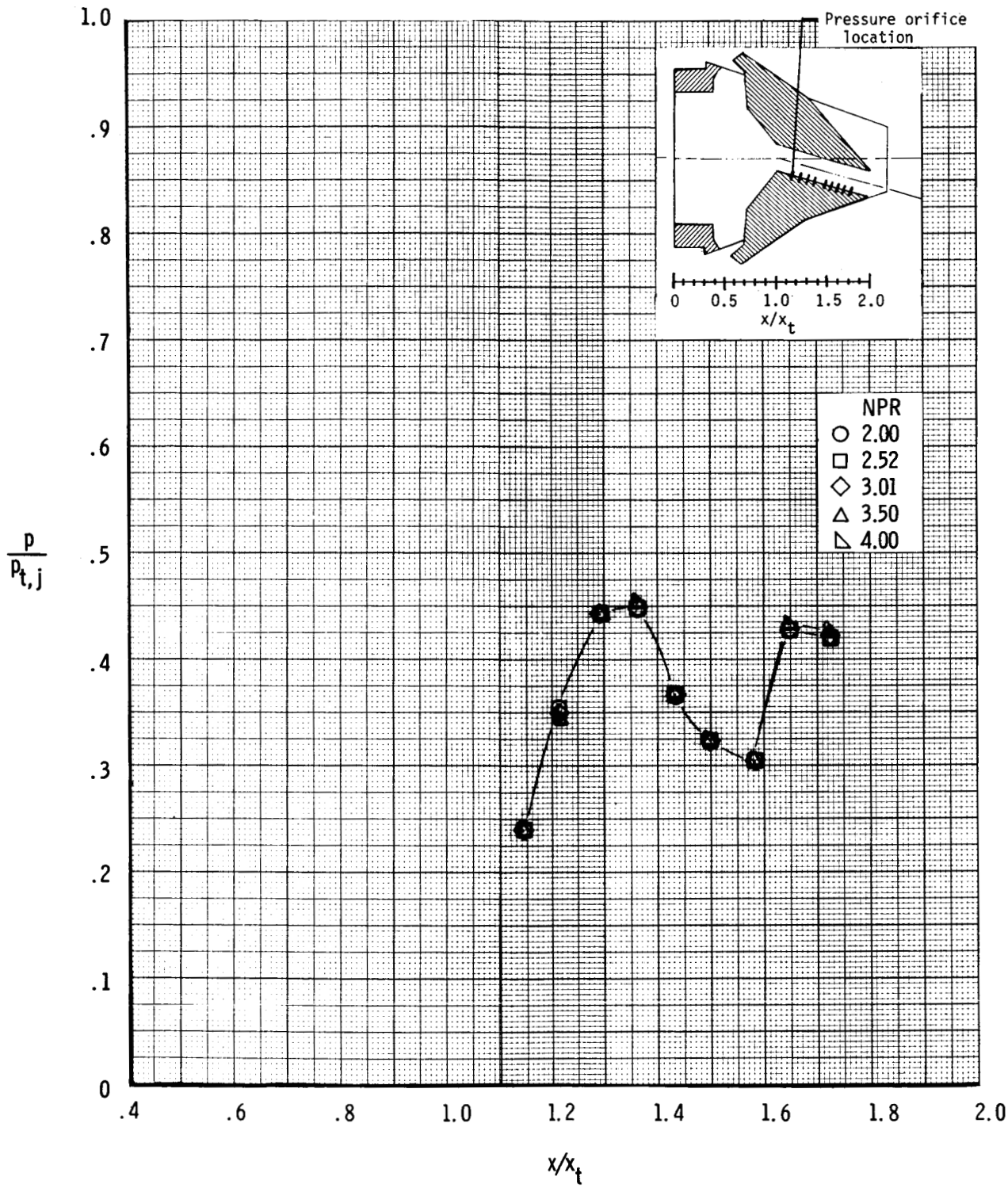

(b) Lower flap centerline pressures.
Figure 7. Continued.

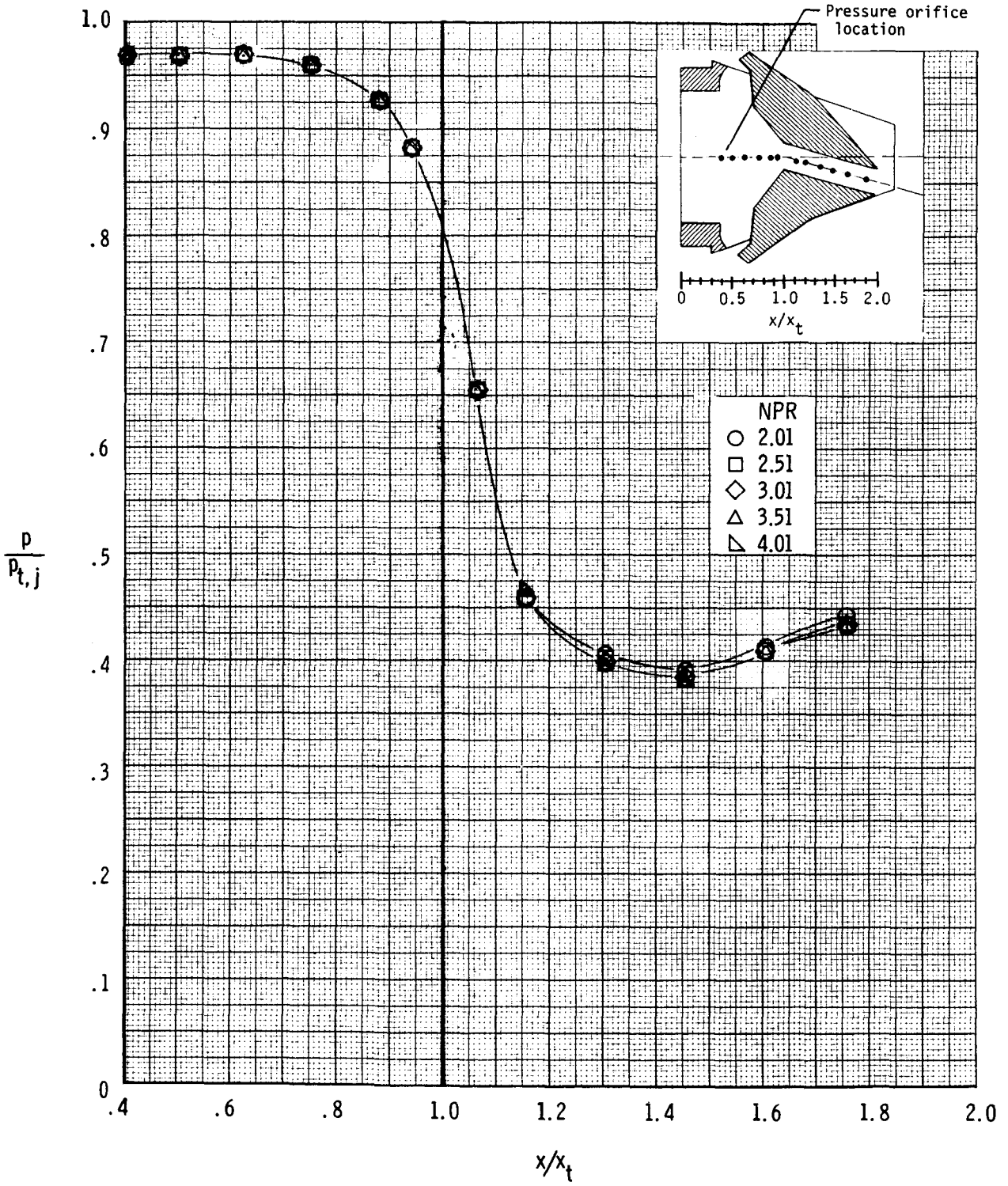

(c) Sidewall centerline pressures; $w/w_t = 0$ for $x/x_t \leq 1.0$; $\eta/\eta_t = 0$ for $x/x_t > 1.0$.
Figure 7. Continued.

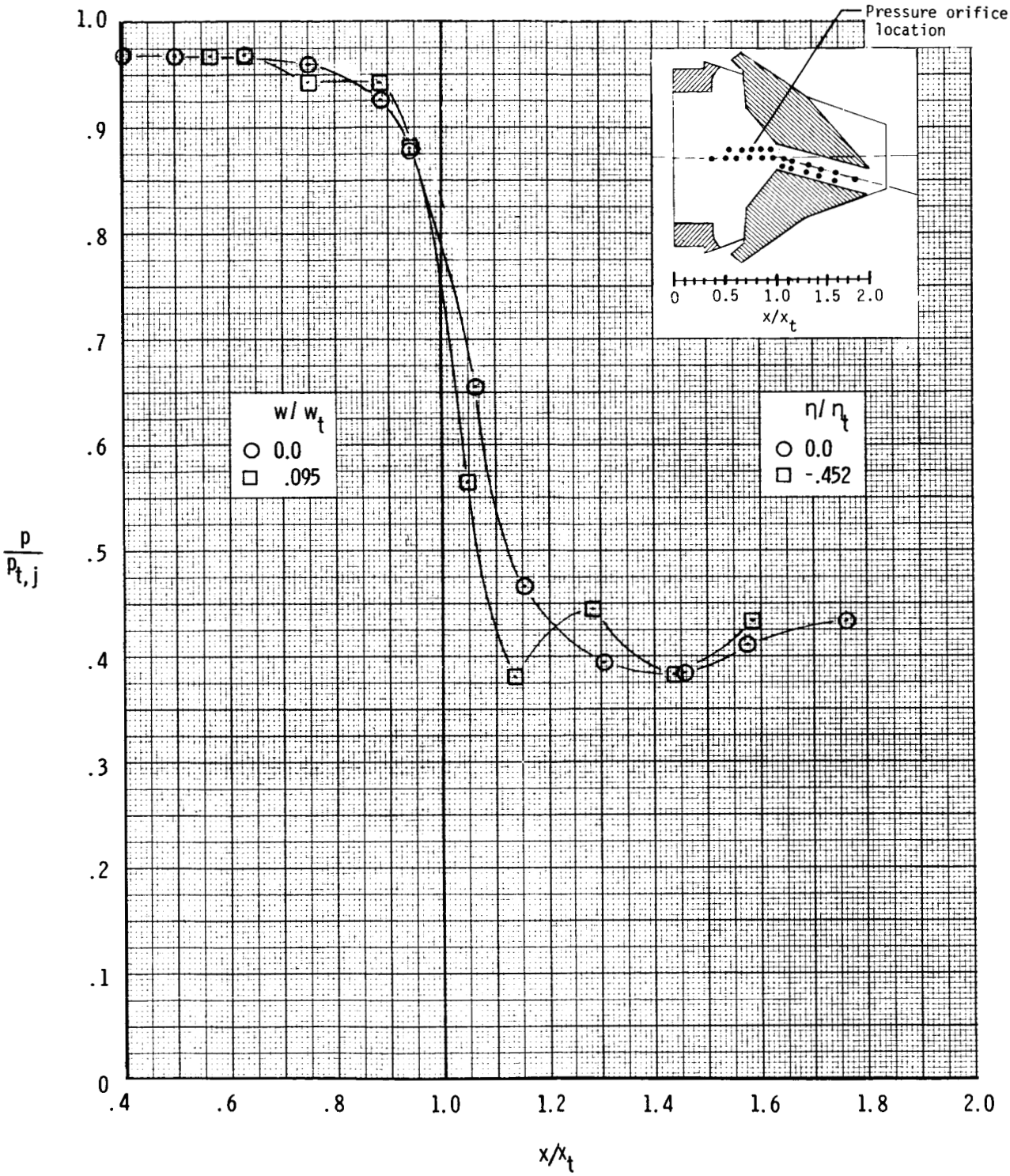

(d) Variation of pressure across nozzle sidewall at NPR = 4.0.

Figure 7. Continued.

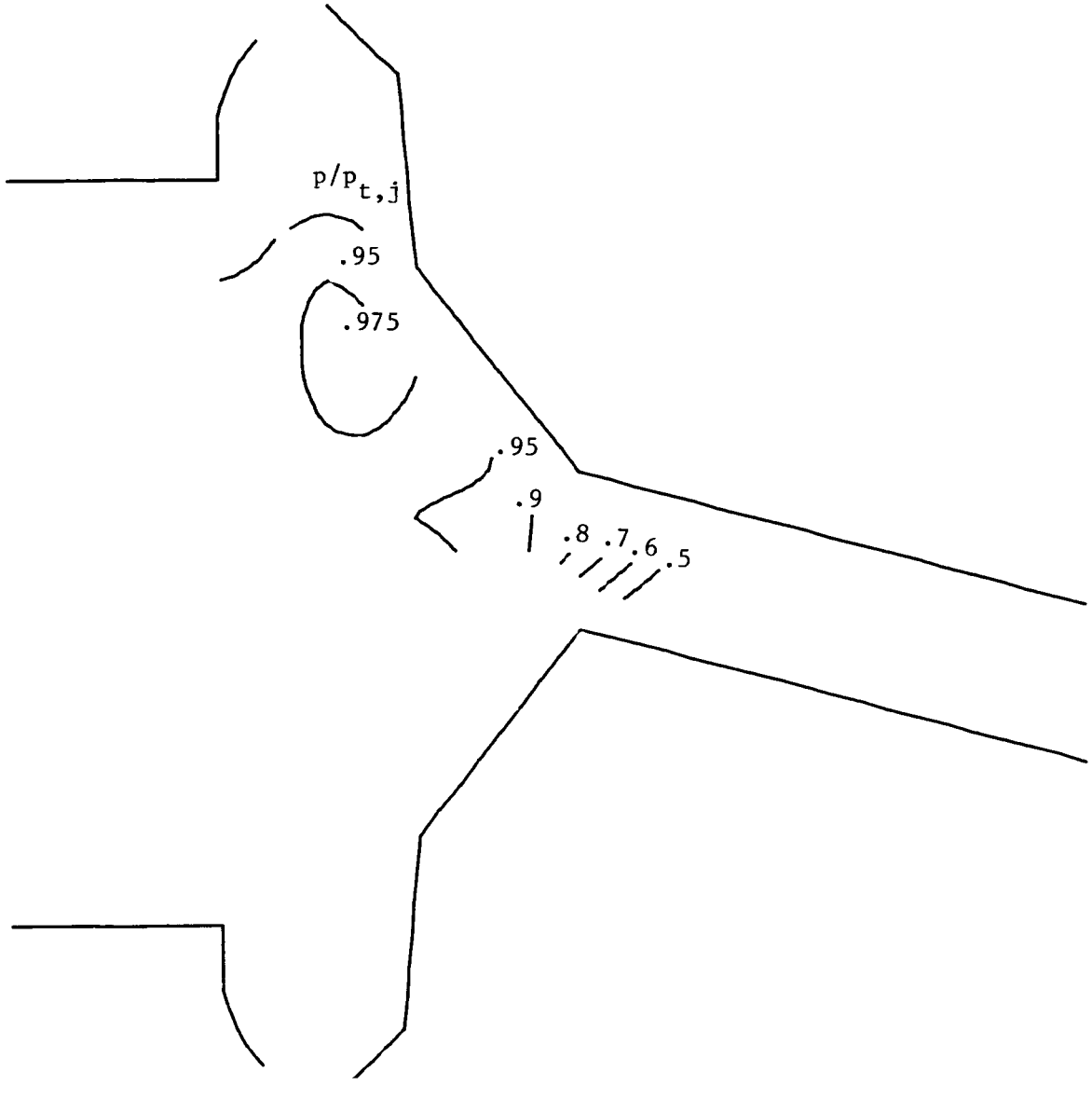

(e) Contours of $p/p_{t,j}$ on 15° vectored nozzle sidewall for NPR = 4.0.
Figure 7. Concluded.

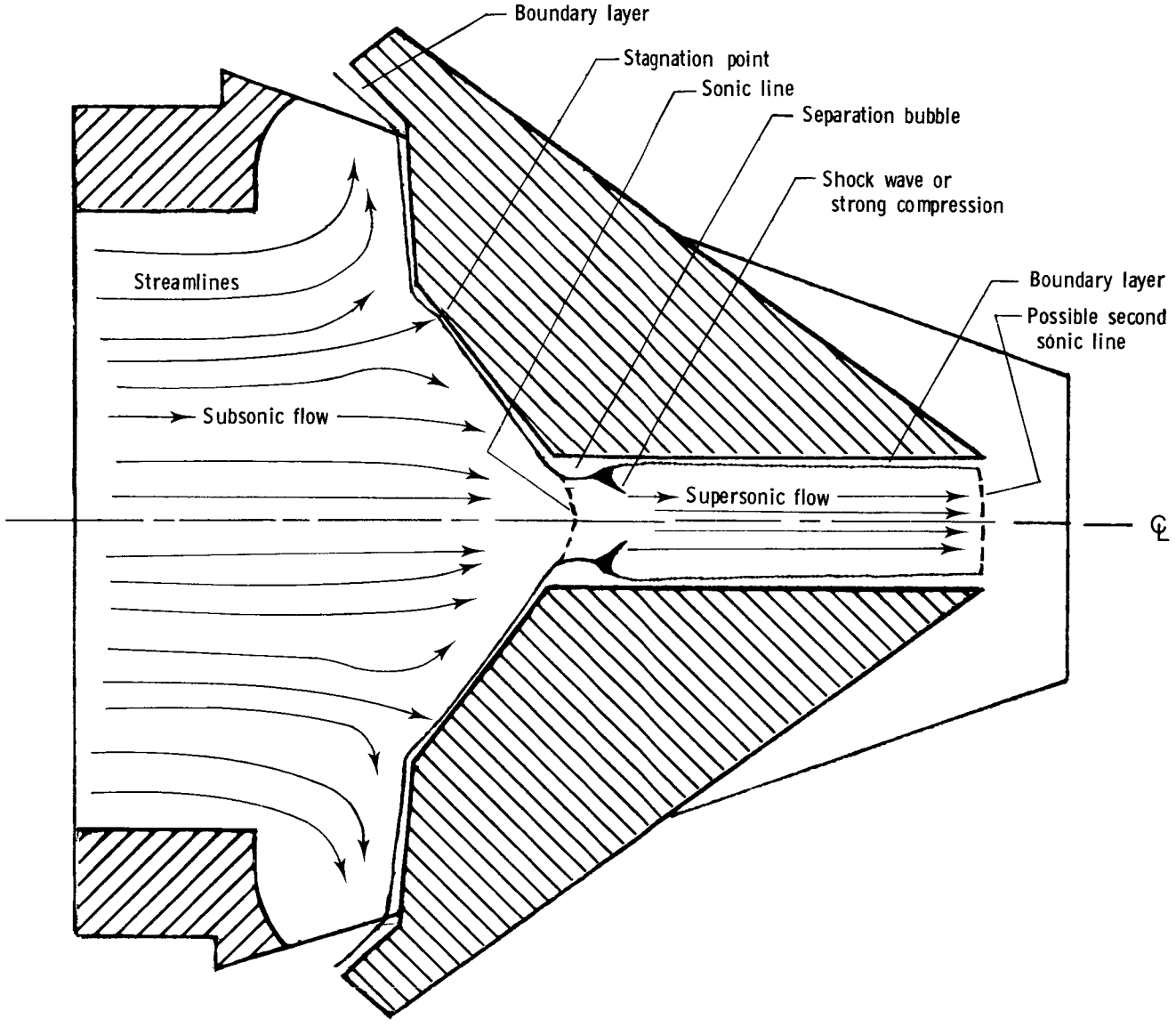

(a) 0° vectored primary flow.

Figure 8. Internal flow phenomena for nozzle with reverser deployed 50 percent.

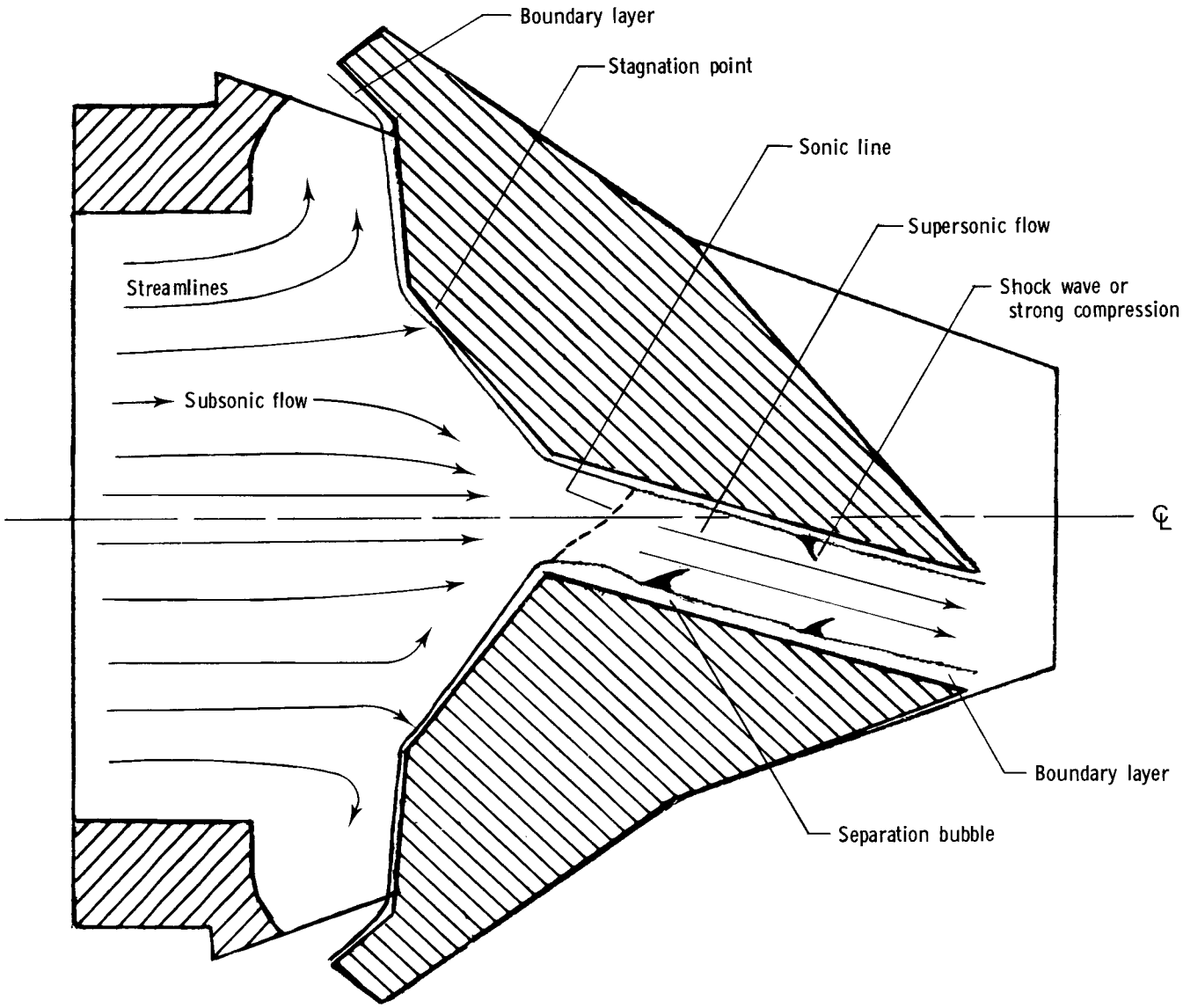

Note:
Supersonic flow in converging duct: velocity decreases, static pressure increases.
Supersonic flow in diverging duct: velocity increases, static pressure decreases.

(b) 15° vectored primary flow.

Figure 8. Concluded.

Standard Bibliographic Page

1. Report No.	2. Government Accession No.	3. Recipient's Catalog No.
NASA TM-89044		

4. Title and Subtitle	5. Report Date
Measured Pressure Distributions Inside Nonaxisymmetric Nozzles With Partially Deployed Thrust Reversers	March 1987
	6. Performing Organization Code: 505-62-91-01
7. Author(s): Robert S. Green and George T. Carson, Jr.	8. Performing Organization Report No.: L-16210
9. Performing Organization Name and Address: NASA Langley Research Center, Hampton, VA 23665-5225	10. Work Unit No.
	11. Contract or Grant No.
12. Sponsoring Agency Name and Address: National Aeronautics and Space Administration, Washington, DC 20546-0001	13. Type of Report and Period Covered: Technical Memorandum
	14. Sponsoring Agency Code

15. Supplementary Notes

Robert S. Green: Wright-Patterson Air Force Base, Dayton, Ohio.
George T. Carson, Jr.: Langley Research Center, Hampton, Virginia.

16. Abstract

An investigation was conducted in the Langley 16-Foot Transonic Tunnel at static conditions to measure the pressure distributions inside a nonaxisymmetric nozzle with simultaneous partial thrust reversing (50-percent deployment) and thrust vectoring of the primary (forward-thrust) nozzle flow. Geometric forward-thrust-vector angles of 0° and 15° were tested. Test data were obtained at static conditions while nozzle pressure ratio was varied from 2.0 to 4.0. Results indicate that, unlike the 0° vector angle nozzle, a complicated, asymmetric exhaust flow pattern exists in the primary-flow exhaust duct of the 15° vectored nozzle.

17. Key Words (Suggested by Authors(s))	18. Distribution Statement
Nonaxisymmetric nozzles Thrust reversing Thrust vectoring	Unclassified—Unlimited Subject Category 02

19. Security Classif.(of this report)	20. Security Classif.(of this page)	21. No. of Pages	22. Price
Unclassified	Unclassified	41	A03

For sale by the National Technical Information Service, Springfield, Virginia 22161